

# Maximum efficiency of perovskite solar cells by material properties tuning and cell design: a multidimensional approach

Manfred G. Kratzenberg<sup>1,2\*</sup>, Ricardo Rüther<sup>2</sup> & Carlos R. Rambo<sup>3</sup>

## Abstract

In order to obtain significant improvements in the Power Conversion Efficiency (PCE) of solar cells, researchers should know in the future which material properties and cell design constitute cells with the highest possible efficiency. Such knowledge can be obtained by simulation and numerical optimization of the cells PCE, which is shown for a Perovskite Solar Cell (PSC) in a multidimensional variable space. By use of a sensitivity analysis, based on the analytical model of a PSC, it is shown that its efficiency is a nonlinear function of several variables in a multidimensional hypercube space. The numerical optimization presented increases the PCE from initially 15.7 % to 27.6 % in a nine-dimensional function space of material properties and absorber layer thickness. Here the combined variable specification necessary to obtain such a high efficiency is presented, and it is discussed how the manufacturing can be improved in order to successfully increase the cells PCE.

.....

Early research in hybrid solar cells<sup>1-3</sup> led to the concept of the perovskite-based solar cell<sup>4</sup>, and more recent advances in searching for new organic-inorganic hybrid semiconductor materials and properties for this type of cell<sup>5-19</sup> provided the steepest increase of power conversion efficiency (PCE) values in comparison to other solar cell types, reaching the state-of-the-art PCE of 22.1%<sup>20</sup>.

<sup>1</sup> Electrical Materials Laboratory (LAMATE), Department of Electrical Engineering, Universidade Federal de Santa Catarina (UFSC), Trindade, PO Box 476, 88040-970 Florianópolis, Santa Catarina (SC), Brazil.

<sup>2</sup>Fotovoltaica UFSC – Solar Energy Research Laboratory, Department of Civil Engineering, Universidade Federal de Santa Catarina (UFSC), Av. Luiz Boiteux Piazza, 1302, Florianópolis, SC, Brazil.

\* e-mail: manfredkratzenberg@gmail.com

A smart combination of these material's properties in a multidimensional optimization can further improve the PCE in single-junction and multi-junction PSCs. Due to the use of low-cost materials and manufacturing methods, it is predicted that future photovoltaic (PV) modules based on PSC might result in the lowest Levelized Cost of Energy (LCOE) if compared to state-of-the-art renewable and non-renewable technologies for the generation of electric energy<sup>21</sup>. In this configuration, solar cells with highly reproducible electrical characteristics<sup>22</sup> and non-degrading efficiency values<sup>23-27</sup> are demanded, resulting, therefore, in low mismatch losses and a long lifetime of photovoltaic modules. Additional cost benefits can be obtained by the PSC's superior band gap tunability<sup>15,27,28</sup>, which enables its use in tuned double-junction solar cell devices<sup>27, 29,30</sup>, resulting in up to 40.6% of PCE<sup>31</sup>, while in tuned triple junction PSC the maximal efficiency is below the thermodynamic limit of 50%<sup>29</sup>.

State-of-the-art PSCs are mostly optimized based on cell prototyping, where the cells are produced based on reasoning and hypothesis testing of assumed physic principles. However, the benefits of mathematical modeling of PV device efficiency, by use of analytical<sup>32-34</sup> or numerical models<sup>35-38</sup>, can give a valuable input, which may further accelerate the development of this cell technology. State-of-the-art modeling leads to the PCE increase as a function of one or two model variables at once, using multidimensional models of material properties and manufacturing specifications<sup>32-38</sup>. In this paper, we numerically optimized the mathematical model of a single junction PSC, which includes multiple model variables. In order to obtain the highest possible cell efficiency, the following fundamental questions should be answered: (i) which multiple model variables can be concomitantly improved in order to obtain the highest efficiency values; (ii) should the value of the variables considered be increased or decreased; (iii) to which specific value each of these model variables should be adjusted; (iv) which variables or properties account for the most significant efficiency

enhancement. At first glance, these questions can only be answered if the multidimensional solar cell model is simulated several times by an exhaustive search method, as suggested by Sun et al.<sup>32</sup>, in order to find the best combination of values, which might eventually lead to the highest efficiency. A numerical model of the solar cell would be almost prohibitive in this case, due to the high computational cost for each simulation, leading to a time demanding optimization process. However, an analytical model is most advantageous because of the reduced computational cost. Furthermore, the approximations made by such a model result in a small fitting error between the measured and the modeled PCE of only 0.1 %<sup>32</sup>, which is insignificant considering that outdoor spectral variations can lead to PCE uncertainties of 3 % in thin film cells<sup>39</sup>. Additionally, by a systematic search method, using the numerical optimization algorithm deployed here, not only a further reduction of the computational cost, but also a solution for the maximum efficiency with high repeatability was obtained. Such an optimization leads to identical values of the material's properties, absorber layer thicknesses and efficiencies for the second decimal case if repeated optimizations are compared.

## **Results**

### **Complete set of one- and two-dimensional optimizations**

We used the analytical model of the PSC as derived analytically in Sun et al.<sup>32</sup>, with a detailed charge transport scheme shown in Fig. 1a. The absorption of light and conversion into charge carriers is modeled by the Beer-Lambert law, where the necessary absorber layer thickness can be reduced as a function of a lower average optical decay length, for a similar solar irradiation conversion (Fig. 1b). In Figs. 2a to 2e a set of one- and two-dimensional sensibility analyses are carried out in order to identify the model variables that result in the most significant efficiency increase with the analytical solar cell model. In order to show the possible combinations of variables in these analyses, a large set of 45 figures would be

necessary considering a nine-dimensional function space. Therefore, the highest attainable efficiency of those figures is presented in Table 1, considering by the introduced boundary expansion factor  $f_B$  (equation 5), different ranges at which the model variables can adapt in order to obtain an efficiency increase. This table was obtained by use of numerical optimizations, and it shows the maximal accomplishable efficiency by any possible one- and two-dimensional optimizations, which increase the efficiency from an initial 15.7 %<sup>32</sup> up to a simulated maximum of 22.5 %.

### **Multidimensional optimization**

The multidimensional optimization approach proposed here is highly valuable, as it results in a superior PCE of 27.56%. As in the two-dimensional optimizations, we have used the material properties as obtained by Sun et al.<sup>32</sup> as an initial configuration of the present numerical optimization (Table 2 – line 1). This was obtained by the following steps: (i) solar cell manufacturing; (ii) measurement of the current-voltage curve (I-V curve) in the dark and under reference light conditions; (iii) model fitting using the measured I-V curves; (iv) one-dimensional thickness optimization of the absorber layer using the analytical model; (v) repeated cell manufacturing with the optimized thickness, (vi) repeated measurement of the I-V curves, and (vii) repeated model fitting. In the present optimizations, we considered flexible ranges of variable improvement, which are specified by the improvement factor  $f_B$  and further criteria that determine the optimization constraints in a single optimization process (equations 4 to 7). These constraints denote the range of the variables with allowed maximum and minimum values for each variable. In this range, it is allowed for the optimization algorithm to modify each one of the nine variables in the task of searching the highest possible PCE. As a result, an ideal constitution of model variable values is obtained. This concept gives hypothetical details in order to demonstrate how the multidimensional

variation of material properties and manufacturing parameters can enhance the two-dimensional optimization approach, and it establishes the actual potential of attainable cell efficiencies. It is proved that the concomitant optimization of the whole set of seven model variables in a multidimensional numerical optimization is more effective when compared to one- or two-dimensional optimizations. The demanded material properties and the absorber layer thickness for the highest simulated efficiency, as selected by the optimization algorithm, are presented in Table 2 – line 6, considering a maximal boundary expansion factor of  $f_B = 160$ . Table 3 and Supplementary Figs. 1 and 2 present the efficiency improvements as a function of the boundary expansion factor  $f_B$ , while Table 3 presents the material properties and the absorber layer thickness. Supplementary Fig. 1 presents the cell efficiencies for several specific combinations of variables, and Supplementary Fig. 2 shows cell efficiencies considering specific minimal thickness limitations inherent to different coating techniques. Fig. 2f shows how the sensitivity analysis of Fig. 2e increases the PCE if optimized variables, as presented in Table 3, are set up in the analytical model, excluding the absorber layer thickness ( $t_0$ ), and the average optical decay length ( $\lambda_{ave}$ ). As result of the multidimensional optimization, the modeled I-V curves are presented in Fig. 3, using  $f_B = 160$ , and normalized solar radiation conditions with an irradiance of  $100 \text{ mW/cm}^2$  and an Air Mass of 1.5. This figure shows how the two I-V curves adapt if the whole set of optimal material properties are used in the analytical solar cell model (Table 2 – line 6), obtaining a maximum PCE of 27.56 %.

## Discussion

In the multidimensional optimization, the efficiency increases mainly by an enhanced open circuit voltage ( $V_{oc}$ ), which leads to a higher maximum power point voltage ( $V_{MPP}$ ). The MPP current ( $I_{MPP}$ ) also increased to some small extent, which is caused by a higher short

circuit current ( $I_{oc}$ ), but mainly due to the increase of the fill factor (FF). The short circuit current usually increases more significantly by band gap tuning, which is not considered in the presented optimization, as the effective band gap of the present PSC is 1.1 eV. This band gap value leads to a theoretical efficiency limit of 32.23 %<sup>40</sup>, which is only 0.68 % lower than the highest Shockley-Queisser thermodynamic efficiency limit for single junction solar cells, which demands an ideal band gap of 1.4 eV<sup>40</sup>. It can be observed for the non-optimized solar cell that the cell current in the dark ( $J_{dark}$ ), which is modeled by use of the back and front recombination currents (Supplementary Equation 5), is almost zero at MPP voltage (Fig. 3), which is advantageous as practically zero recombination losses can be considered for the MPP operation point. Conversely, the model obtained by the present optimization exhibits slightly higher recombination losses, presenting a  $J_{dark-max} = -0.05 \text{ mA/cm}^2$  at  $V_{MPP}$  (Fig. 3). However, this small recombination loss increase is outweighed by the steep efficiency increase in case of the multidimensional optimization, resulting in an optimized efficiency of 27.56 %.

### **Ideal constitution of a perovskite solar cell**

An ideal solar cell device has the lowest possible front and back ( $s_f$ ,  $s_b$ ) surface recombination velocities, and the lowest possible average optical decay length ( $\lambda_{ave}$ ), resulting in an optimized modification factor of 1/160 for these three variables (Table 2 – line 7). This is intuitive as the lowest  $s_f$ ,  $s_b$  lead to the lowest charge carrier recombination, and the lowest  $\lambda_{ave}$  leads to the highest solar radiation absorption and conversion into charge carriers. The diffusion coefficients of electrons ( $D_n$ ) and holes ( $D_p$ ) are adjusted to their upper boundary values by a modification factor of 160, which is also expected as larger diffusion coefficients result in longer electron and hole diffusion paths before recombination occurs and, therefore, the probability of recombination is reduced. The excess concentration

of electrons and holes  $\Delta n$  and  $\Delta p$  were not modified by the numerical optimization algorithm, as their values are already located within the region where the efficiency is highest (Fig. 2d). The built-in voltage ( $V_{bi}$ ) is adjusted to its upper limit of 1.4 V (equation 6) by the optimization algorithm. It is found that the absorber layer thickness is optimized to a specific value of 4.1 nm (Table 2 – line 6) and not to its lower boundary value of 2.8 nm (Table 2 – line 2). This is evident as the absorber layer thickness stands in close relationship with the average optical decay length  $\lambda_{ave}$  (Fig. 1b), and therefore, it has always to be adjusted as a function of the obtained  $\lambda_{ave}$ , both in a two-dimensional optimization (Fig. 2e), as well as in a multidimensional optimization (Fig. 2f), as shown by the blue vertex lines in these figures. As expected, the highest efficiency of 27.56% obtained here (Table 2 – line 6) is higher than the highest state-of-the-art maximum efficiency of 25 %<sup>33,37</sup>, but is lower than the Shockley-Queisser thermodynamic limit for single junction solar cells<sup>40</sup>. It has to be remembered that the concomitant property improvement obtained here, which results in a PCE of 27.56 % (Table 2 – line 6), represents an ideal case. The cell efficiency of manufactured solar cells may only approximate this ideal PCE, as the set of material's properties in future research will probably not be improved by such high improvement factors of  $f_B = 160$  within the same cell. For that reason, Table 3 presents the obtainable efficiency values as a function of different boundary expansion factors resulting in different necessary material properties, showing thus a possible pathway for efficiency improvement in future cell manufacturing. As the highest gradients of efficiency improvement are obtained for small  $f_B$  values (Supplementary Figs. 1 and 2) only half of the improvement, with  $f_B = 80$ , results in the most significant efficiency improvement leading to a PCE of 27.25 % (Table 3).

## Effect of the absorber layer thickness

PSCs stand out by the fact that they can be manufactured by a number of different low-cost manufacturing methods<sup>41-43</sup>. Some of these methods, e.g. the solvent-solvent extraction method<sup>44</sup>, allow perovskite coatings with very low thickness down to 20 nm without the presence of pinholes, while the minimum thickness for other methods, especially printing techniques<sup>43</sup> is much higher. Thus, each coating method has its proper minimum thickness limitation for the absorber layer ( $t_{0-\min}$ ) in order to mitigate pinholes, which would otherwise increase the shunt resistance and, consequently, decrease the solar cell efficiency<sup>45</sup>. Therefore, it is crucial to know how thickness constraints reduce the highest obtainable efficiency values for different boundary expansion factors ( $f_B$ ). Therefore, in Supplementary Section S3 several multidimensional optimizations sets with different  $f_B$  factors are considered, and additionally, individual thickness constraints are imposed on the absorber layer thickness (Supplementary Fig. S2). As seen in this figure the absorber layer thickness reduction can raise cell efficiencies by up to 2.2 %. An ideal thickness of the absorber layer is in the order of 6 to 20 nm, whereas thicknesses up to 40 nm lead to depreciable efficiency losses when very high or very low improvement factors  $f_B$  for the remaining model variables are considered. It should be emphasized that such thin absorber layers only make sense if paired with extra small  $\lambda_{ave}$  values, which can be obtained, for instance, by insertion of plasmonic nanoparticles into the absorber layer, increasing, therefore, the light trapping effect as a function of the cells increased solar irradiation absorption and conversion<sup>46</sup>. Meanwhile, the addition of a large number of plasmonic nanoparticles may lead, on its own, to further local recombination effects, which are supposed to be accentuated especially in very thin absorber layers, by reason of the larger density of the plasmonic metal particles that may lead to undesired conduction effects<sup>46</sup>. Therefore, the efficiency loss by



means of pinholes and plasmonic nanoparticles has to be identified and analyzed by independent methods in future research.

The highest attainable efficiency values appear for thin absorber layers ( $t_0$ ), e.g. 30 nm in Fig. 2f, as shown by the lowest point of the blue vertex line, with  $\lambda_{ave}$  of  $\sim 5$  nm. Nevertheless, it can be seen that already high cell efficiencies, of approximately 23 %, appear for absorber layer thicknesses from 510 to 800 nm for any  $\lambda_{ave}$  value, as shown by the large red-brown and brown area in Fig. 2f. This means that considering an unchanged  $\lambda_{ave}$  of 100 nm, no additional light trapping effects are necessary to obtain high cell efficiencies of approximately 23 % if the remaining model variables can be improved. However, an ideal absorber layer thickness for  $\lambda_{ave} = 100$  nm is  $t_0 = 550$  nm in this specific case (Fig. 2f). If light trapping effects result in values of  $\lambda_{ave} < 40$  nm, then the efficiency can be increased to values up to 24 % (dark-brown area in Fig. 2b), considering an absorber layer thicknesses  $< 210$  nm. Table 1 reveals that  $D_n$  and  $s_f$  are the most sensible variables, showing in a one-dimensional optimization an efficiency increase from 15.7 % to 18.4 %, for a boundary expansion factor of  $f_B = 100$ . Considering all possible combinations of two-dimensional optimizations, this efficiency increases to 22.5 % if the front and back layer surface recombination velocities are reduced. Meanwhile, the multidimensional optimization proposed here presents a significantly higher development potential in comparison with one- and two-dimensional optimizations, increasing the solar cell's efficiency to 27.44 % for the same  $f_B$  (Table 3).

## Conclusions

We presented for the first time a numerical optimization and a complete sensitivity analysis of a multidimensional analytic PSC model. Such an optimization is of importance in order

to show in which proportion cell efficiencies can be increased by the concomitant optimization of several material properties and the absorber layer thickness. The specific demands for the material properties and the absorber layer thickness of the highest efficiency PSC were defined, and it is discussed, in Supplementary Section S3, how these properties can be manipulated by appropriate manufacturing methods and material use. The behavior of the analytical model of the pin-type PSC proves that this cell type has a high development potential, as its efficiency was increased from 15.7 % to a maximum of 27.56 % by the present simulation-based optimizations. While it is not sure at the present if such a high efficiency can be obtained in practice, the most important contributions in this paper are the complete specifications of the necessary material properties and absorber layer thickness in order to optimize cell efficiencies at several scales. These estimated values by the present optimizations are based on simulations with a deterministic solar cell model and give an outlook for future research activities. Here, an improved understanding of the PSC was also obtained by the one- and two-dimensional sensibility analyses and optimizations. It was found that the cell thickness has to be optimized as a function of the current or a shorter average optical decay length in both two-dimensional and multidimensional optimization processes. However, the multidimensional optimization leads to a much higher PCE. Interestingly, the thickness reduction of the absorber layer caused not only an efficiency increase but also led to a reduced perovskite material use and therefore, an order of magnitude lower quantity of lead (Pb) residuals. This lower residual content places the perovskite solar cell proposed here in a favorable position, as state-of-the-art PSCs contain already a low quantity of heavy metal residuals, which is similar to state-of-the-art photovoltaic modules<sup>47,48</sup> which present e.g. 90-300 times lower heavy-metal content in its life cycle analysis compared to coal-fired power plants<sup>49</sup>. In order to increase cell efficiencies most effectively, the calculated specifications of material properties, for

different PCE (Table 3), results in specific recommendations for the cell's manufacturing process and material use in future research, which are inferred from the results of the presented optimizations in combination state-of-the-art knowledge in PSC manufacturing (Supplementary Sections S2 and S3).

## Methods

The analytical model of the pin-type PSC (Supplementary Section S1) simulates the solar cell current as a function of the terminal voltage and its material properties, thus obtaining its I-V curve in the dark, located in the fourth Cartesian quadrant (Fig. 3). Under exposure to a reference solar irradiance, a second I-V curve is obtained, which appears in the first Cartesian quadrant. From the I-V curve obtained in the first quadrant, the power curve is calculated and its maximization results in the Maximal Power Point, for which the solar cell efficiency was calculated. The initial model variables ( $X_1 \dots X_9$ ) were obtained by a fitting model, which manipulates the material's properties and absorber layer thickness values in a form that the shape of the modeled I-V curves is similar to the measured I-V curves shape<sup>32</sup> of a manufactured solar cell. Here the numerical optimization of this analytical model in a multidimensional function space is proposed, which is specified by the following optimization problem.

$$\eta_{\max} \rightarrow \max [\eta_i(X_{1,i} \dots X_{9,i})] ; i = 1 \dots N \quad (1)$$

Where the efficiency  $\eta_i$  at the  $i$ -th maximization iteration is a function of the nine PSC model variables ( $X_{1,i} \dots X_{9,i}$ ), which built-up a nine-dimensional hypercube space of model variables, and where the maximum efficiency ( $\eta_{\max}$ ) is obtained after  $i = 1 \dots N$  model simulations and variable modification steps. In each of the  $i$  steps, the Matlab<sup>TM</sup> optimization algorithm *fmincon* improves the values of the whole set of model variables by means of the combination of several sophisticated Nonlinear Programming (NP) optimization techniques in order to obtain the maximal possible model efficiency. When the increase of the efficiency of the cell is below a considered threshold value, the optimization algorithm considers that the maximal cell efficiency is obtained, for a specified set of variable ranges of the model variables, and the algorithm stops the optimization process. A new calculation of the I-V curves, the Maximum Power Point Power, and the cell's efficiency ( $\eta_i$ ) is accomplished at each model simulation  $i$ , using equation (2). This cell efficiency is calculated as a function of the model variables  $X_{1,i}$  to  $X_{9,i}$ , which are constituted by eight quantum physical material properties and the absorber layer thickness.

$$\eta_{MPP,i} = (U_{MPP,i} J_{MPP,i}(X_{1,i} \dots X_{9,i})) / G_{AM1.5} = P_{MPP,i} / G_{AM1.5} \quad (2)$$

In equation (2)  $G_{AM1.5} = 100 \text{ mW/cm}^2$  is the normalized solar irradiation at Air Mass 1.5. The solar cell's output power  $P_{MPP,i} [\text{mW/m}^2]$  of the  $i$ -th optimization step (equation 2) is obtained by the maximization of its power curve. The one-dimensional optimization of the solar cell's power curve uses  $k = 1 \dots M$  iterative steps, which identify its MPP - power ( $P_{MPP,i}$ ) as follows.

$$P_{MPP,i} \rightarrow \max (P_k (J_{light,k} (G_{AM1.5}, V_k, X_{1,i} \dots X_{9,i}) \dots J_{kM}(G_{AM1.5}, V_k)) ; k = 1 \dots M \quad (3)$$

The analytical model of the solar cell uses the whole set of model variables ( $X_{1,i} \dots X_{9,i}$ ) as well as the terminal voltage ( $V_k$ ) and the cell's temperature as input variables and calculates the solar cell's current  $J_{light,k}$  (Fig. 3) under exposure to reference light ( $G_{AM1.5}$ ). Then  $J_{light,k}(G, V)$  and the terminal voltage  $V = V_k$  are adopted as  $k$ -th voltage and current in an optimization of the solar cells I-V curve (Supplementary Equation 3), needing  $k = 1 \dots M$  optimization steps. The power optimization of equation (3) is nested in the efficiency optimization in equation (1) and the optimization process presented here is subject to the following specific boundary conditions:

$$X_{j,min} \leq X_j \leq X_{j,max} , j = 1 \dots 9 \quad (4)$$

Where  $X_{j,max}$  and  $X_{j,min}$  are the maximal and minimal constraints for each one of the nine model variables  $X_j$  to be optimized. The more specific model variable constraints for a single optimization process are given by equation (5). Considering that the  $j = 1 \dots 9$  model variables can only be improved within a limited range of ( $X_{j,min} \dots X_{j,max}$ ), each single optimization process considers an individual boundary expansion. We consider that most of the variables do not have specific improvement limitation as a result of a related state-of-the-art theory, and therefore, the sets of boundary conditions are defined equally for the whole set of model variables. This general boundary expansion is operated by the unitless expansion factors  $f_B$  as given by the equation of the constraints as follows.

$$X_{j,min} = (1/f_B) X_{j,me} \leq X_j \leq X_{j,me} (f_B) = X_{j,max} ; j = 1 \dots 9 \quad (5)$$

Where  $f_B$  and  $1/f_B$  specify the individual amplification and reduction factors in a single optimization process, which result in the values of the upper and lower boundary limits for the model variables ( $X_{j,min}$  and  $X_{j,min}$ ) in that specific efficiency optimization. In equation (5)  $X_{j,me}$  represents the not expanded initial configuration of

the model variables, as measured by Sun et al.<sup>32</sup> and  $X_{j-\min}$  and  $X_{j-\max}$  are the minimum and maximum limits specified in equation (4). As built-in voltages ( $V_{bi} > 1.4$  V) do not lead to any further increase cell's efficiency (Fig. 2b), the inequality constraint ( $V_{bi} \leq 1.4$  V) is here additionally imposed in order to avoid unrealistic high values of the variable  $V_{bi}$  (equation 6). Furthermore, as each of the different coating techniques used during the absorber layer deposition needs a specific minimal thickness ( $t_{0-\min}$ ) in order to avoid pinholes and other undesired effects, another additional constraint is given for  $t_0$ , which considers a variable minimum thickness ( $t_{0-\min}$ ) in each one of the optimization processes. The upper boundary is given by a maximum layer thickness of 1  $\mu\text{m}$  as considered in equation (7).

$$0 \leq V_{bi} \leq 1.4 \text{ V} \quad (6)$$

$$t_{0-\min} \geq t_0 \geq 1 \mu\text{m} \quad (7)$$

## References

1. Coutts, T., Li, X., Wanlass, M., Emery, K. & Gessert, T. Hybrid solar cells based on dc magnetron sputtered films of n-ITO on APMOVPE grown P-inP. *In Photovoltaic Specialists Conference, 1988., Conference Record of the Twentieth IEEE*, 660–665 (1988).
2. O'Regan, B. & Grätzel, M. A low-cost, high-efficiency solar cell based on dye-sensitized colloidal TiO<sub>2</sub> films. *Nature* **353**, 737–740 (1991).
3. Wong, W.-Y. *et al.* Metallated conjugated polymers as a new avenue towards high-efficiency polymer solar cells. *Nature Materials* **6**, 521–527 (2007).
4. Kojima, A. *et al.* Organometal Halide Perovskites as Visible-Light Sensitizers for Photovoltaic Cells. *Journal of the American Chemical Society* **131-17**, 6050–6051 (2009).
5. Loi, M. A. & Hummelen, J. C. Hybrid solar cells: Perovskites under the sun. *Nature Materials* **12**, 1087 (2013).
6. Grätzel, M. The light and shade of perovskite solar cells. *Nature Materials* **13**, 838–84 (2014).
7. Marchioro, A. *et al.* Unravelling the mechanism of photoinduced charge transfer processes in lead iodide perovskite solar cells. *Nature Photonics* **8**, 250–255 (2014).
8. D'Innocenzo, V. *et al.* Excitons versus free charges in organo-lead tri-halide perovskites. *Nature Communications* **5** (2014).
9. Yang, Y. *et al.* Low surface recombination velocity in solution-grown CH<sub>3</sub>NH<sub>3</sub>PbBr<sub>3</sub> perovskite single crystal. *Nature Communications* **6** (2015).
10. Zhang, W., Eperon, G. E. & Snaith, H. J. Metal halide perovskites for energy applications. *Nature Energy* **1**, 16048 (2016).
11. Abate, A. *et al.* Supramolecular halogen bond passivation of organic–inorganic halide perovskite solar cells. *Nano Letters* **14**, 3247–3254 (2014).
12. Edri, E. *et al.*, Elucidating the charge carrier separation and working mechanism of CH<sub>3</sub>NH<sub>3</sub>PbI<sub>3-x</sub>Cl<sub>x</sub> perovskite solar cells. *Nature Communications* **5**, 1-8 (2014).
13. Song, D. *et al.* Managing carrier lifetime and doping property of lead halide perovskite by post-annealing processes for highly efficient perovskite solar cells. *The Journal of Physical Chemistry C* **119**, 22812–22819 (2015).
14. Yin, W.-J., Shi, T. & Yan, Y. Unique properties of halide perovskites as possible origins of the superior solar cell performance. *Advanced Materials* **26**, 4653–4658 (2014).
15. Eperon, G. E. *et al.* Formamidinium lead trihalide: a broadly tunable perovskite for

- efficient planar heterojunction solar cells. *Energy & Environmental Science* **7**, 982–988 (2014).
16. Xing, G. et al. Long-range balanced electron and hole transport lengths in organic-inorganic  $\text{CH}_3\text{NH}_3\text{PbI}_3$ . *Science* **342**, 344–347 (2013).
  17. Hsu, H.-L. et al. Enhanced efficiency of organic and perovskite photovoltaics from shape- dependent broadband plasmonic effects of silver nanoplates. *Solar Energy Materials and Solar Cells* **140**, 224–231 (2015).
  18. Cai, B., Peng, Y., Cheng, Y.-B. & Gu, M. 4-fold photocurrent enhancement in ultrathin nanoplasmonic perovskite solar cells. *Optics Express* **23**, A1700–A1706 (2015).
  19. Zhu, L. et al. Temperature-assisted controlling morphology and charge transport property for highly efficient perovskite solar cells. *Nano Energy* **15**, 540–548 (2015).
  20. NREL. Best research-cell efficiencies. *NREL - Photovoltaic Research Homepage* (2017).
  21. Cai, M. et al. Cost-performance analysis of perovskite solar modules. *Advanced Science* **4** (2017).
  22. Ahn, N. et al. Highly reproducible perovskite solar cells with average efficiency of 18.3% and best efficiency of 19.7% fabricated via Lewis base adduct of lead (ii) iodide. *Journal of the American Chemical Society* **137**, 8696–8699 (2015).
  23. Park, N.-G., Grätzel, M., Miyasaka, T., Zhu, K. & Emery, K. Towards stable and commercially available perovskite solar cells. *Nature Energy* **1**, 16152 (2016).
  24. Kaltenbrunner, M. et al. Flexible high power-per-weight perovskite solar cells with chromium oxide-metal contacts for improved stability in air. *Nature Materials* **14**, 1032–1039 (2015).
  25. You, J. et al. Improved air stability of perovskite solar cells via solution-processed metal oxide transport layers. *Nature Nanotechnology* **11**, 75–81 (2016).
  26. Yang, S. et al. Functionalization of perovskite thin films with moisture-tolerant molecules. *Nature Energy* **1**, 15016 (2016).
  27. Bush, K. A. et al. 23.6%-efficient monolithic perovskite/silicon tandem solar cells with improved stability. *Nature Energy* **2**, 17009 (2017).
  28. Huang, H. et al. Colloidal lead halide perovskite nanocrystals: synthesis, optical properties and applications. *NPG Asia Materials* **8** (2016).
  29. Albrecht, S. & Rech, B. Perovskite solar cells: On top of commercial photovoltaics. *Nature Energy* **2**, 16196 (2017).
  30. Bailie, C. D. et al. Semi-transparent perovskite solar cells for tandems with silicon and CIGS. *Energy & Environmental Science* **8**, 956–963 (2015).
  31. Almansouri, I., Ho-Baillie, A. & Green, M. A. Ultimate efficiency limit of single-

- junction perovskite and dual-junction perovskite/silicon two-terminal devices. *Japanese Journal of Applied Physics* **54**, 08KD04 (2015).
32. Sun, X., Asadpour, R., Nie, W., Mohite, A. D. & Alam, M. A. A physics-based analytical model for perovskite solar cells. *IEEE Journal of Photovoltaics* **5**, 1389–1394 (2015).
  33. Agarwal, S. & Nair, P. R. Performance optimization for perovskite-based solar cells. In *Photovoltaic Specialist Conference (PVSC), 2014 IEEE 40th*, 1515–1518 (IEEE, 2014).
  34. Taretto, K., Soldera, M. & Koffman-Frischknecht, A. Material parameters and perspectives for efficiency improvements in perovskite solar cells obtained by analytical modeling. *IEEE Journal of Photovoltaics* **7**, 206–213 (2017).
  35. Foster, J. M., Snaith, H. J., Leijtens, T. & Richardson, G. A model for the operation of perovskite-based hybrid solar cells: formulation, analysis, and comparison to experiment. *SIAM Journal on Applied Mathematics* **74**, 1935–1966 (2014).
  36. Liu, F. et al. Numerical simulation: toward the design of high-efficiency planar perovskite solar cells. *Applied Physics Letters* **104**, 253508 (2014).
  37. Agarwal, S. & Nair, P. R. Device engineering of perovskite solar cells to achieve near ideal efficiency. *Applied Physics Letters* **107**, 123901 (2015).
  38. Wang, F., Chen, Y., Han, G., Zhang, Q. & Ma, Q. The interface and its role in carrier transfer/recombination dynamics for the planar perovskite solar cells prepared under fully open air conditions. *Current Applied Physics* **16**, 1353–1363 (2016).
  39. Rüther, R., Kleiss, G. & Reiche, K. Spectral effects on amorphous silicon solar module fill factors. *Solar Energy Materials and Solar Cells* **71**, 375–385 (2002).
  40. Rühle, S. Tabulated values of the Shockley–Queisser limit for single junction solar cells. *Solar Energy* **130**, 139–147 (2016).
  41. Brittman, S., Adhyaksa, G. W. P. & Garnett, E. C. The expanding world of hybrid perovskites: materials properties and emerging applications. *MRS Communications* **5**, 7–26 (2015).
  42. Burschka, J. et al. Sequential deposition as a route to high-performance perovskite-sensitized solar cells. *Nature* **499**, 316–319 (2013).
  43. Rong, Y. et al. Synergy of ammonium chloride and moisture on perovskite crystallization for efficient printable mesoscopic solar cells. *Nature Communications* **8** (2017).
  44. Zhou, Y. et al. Room-temperature crystallization of hybrid-perovskite thin films via solvent–solvent extraction for high-performance solar cells. *Journal of Materials Chemistry A* **3**, 8178–8184 (2015).
  45. Wu, Y. et al. Highly compact TiO<sub>2</sub> layer for efficient hole-blocking in perovskite



- solar cells. *Applied Physics Express* **7**, 052301 (2014).
46. Atwater, H. A. & Polman, A. Plasmonics for improved photovoltaic devices. *Nature Materials* **9**, 205–213 (2010).
  47. Stasiulionis, J. Life cycle assessment of perovskite solar cells and comparison to silicon solar cells, *Master thesis, Chalmers University of Technology, Gothenburg, Sweden* (2015).
  48. Green, M. A., Ho-Baillie, A. & Snaith, H. J. The emergence of perovskite solar cells. *Nature Photonics* **8**, 506–514 (2014).
  49. Fthenakis, V. M., Kim, H. C. & Alsema, E. Emissions from Photovoltaic life cycles. *Environmental Science & Technology*, **42** 2168–2174 (2008).

## Acknowledgements

The authors thank CNPQ, Brazil and Agência Nacional de Energia Elétrica (ANEEL, Brazil) for their financial support.

## Authors contributions

M.G.K designed the numerical experiments, accomplished the numerical simulations and wrote the manuscript. R.R. discussed specific solar cell efficiency loss mechanisms. C.R.R. discussed specific details about the mathematical model, the understandings of the physical and the chemical details of organic-inorganic perovskite solar cells, presentation of the results and strategy of publication. C.R.R. and R.R. revised, corrected and approved the manuscript. All authors discussed the obtained results equally.

## Additional information

Supplementary information is available in the online version of the paper. Correspondence and requests for materials should be addressed to M.G.K.

## Competing financial interests

The authors declare no competing financial interests.

.

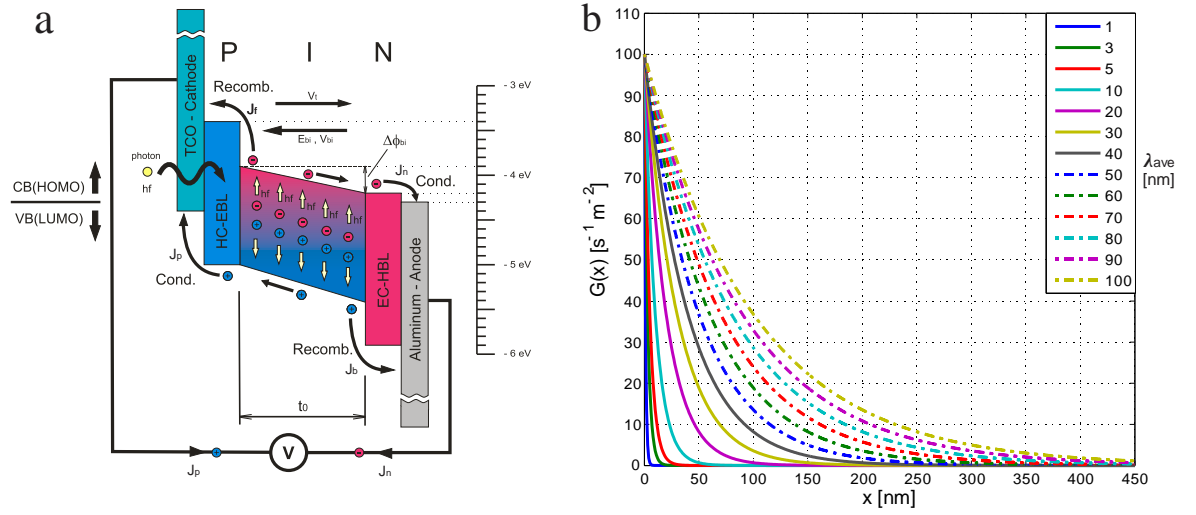


**Figure 1 | Energy band diagram and normalized charge generation.** **a**, Energy potential diagram and charge carrier trajectories of a planar pin-type heterojunction perovskite solar cell with the following components from left to right: (i) transparent cover (here not visible and not considered in the simulations); (ii) cathode layer made of a Transparent Conductive Oxide (TCO); (iii) p-type hole conduction and electron blocking layer made of organic material PEDOT:PSS; (iv) i-type intrinsic charge generation layer with thickness  $t_0 = 450$  nm made of hybrid perovskite material; (v) n-type electron conduction and hole blocking layer made of organic material PCBM; (vi) anode layer made of aluminum. **b**, Approximation of the normalized charge generation profiles  $G(x)$  [ $\text{cm}^{-2}\text{s}^{-1}$ ] per solar cell area and time as a function of the penetration depth from  $x = 0 \dots 450$  nm on the abscissa for several of the considered average optical decay lengths  $\lambda_{\text{ave}}$  [nm] with values within the range of 5 to 150 nm.

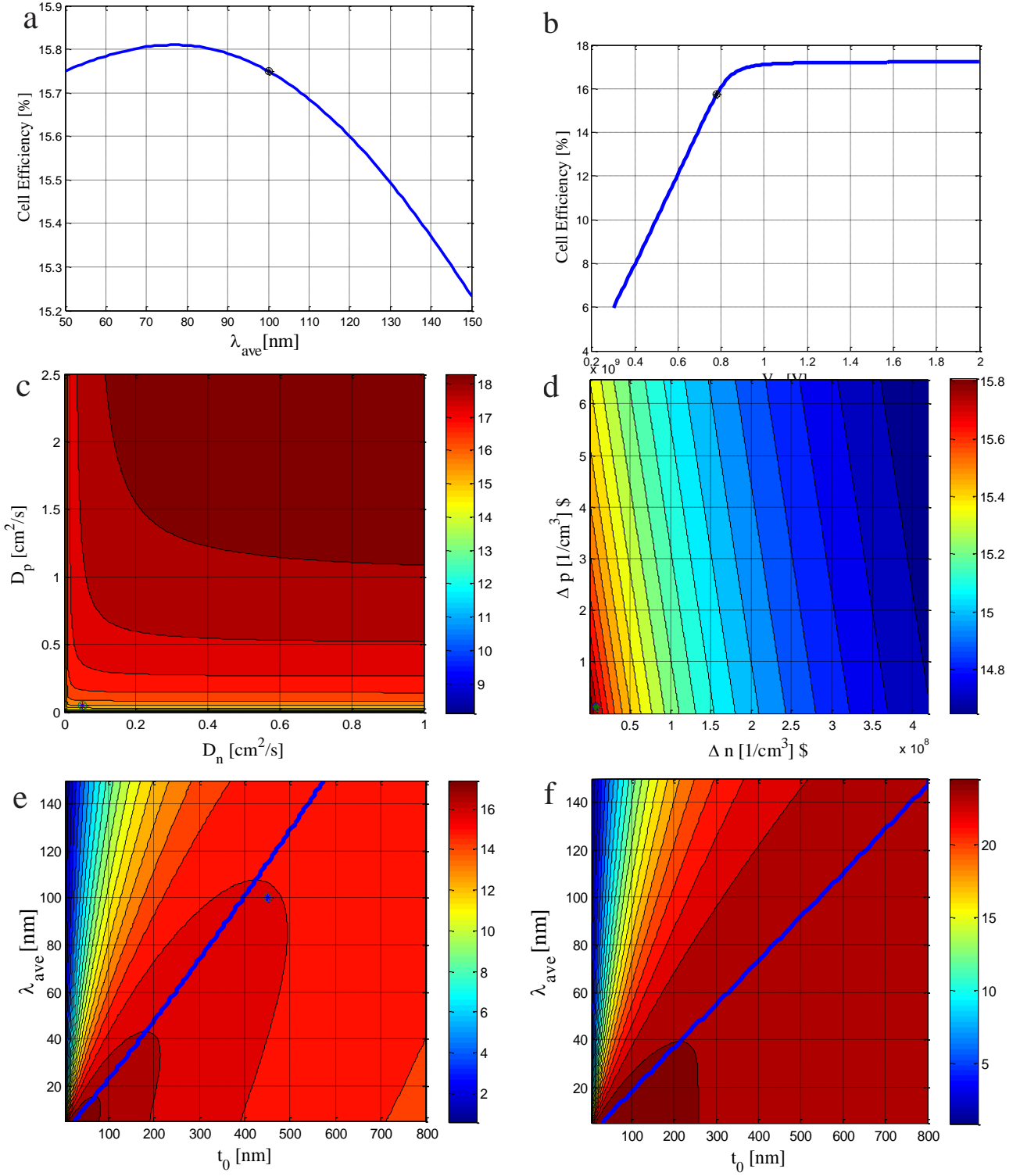


**Figure 2 | Sensitivity analysis of the PCE.** One and two-dimensional sensibility analyses, showing the model efficiency as a function of (the measured efficiency values of 15.7 %<sup>32</sup> are marked by a star within a circle): **a**, average optical decay length; **b**, built-in voltage; **c**, diffusion coefficients of holes and electrons; **d**, excess concentration of electrons and holes; **e**, **f**, absorber layer thickness and average optical decay length, with the blue vertex line showing the maximal attainable efficiency; **a – e**, The remaining model variables are set up to the values obtained in Sun et al. 2015<sup>32</sup>; **f**, The values of the remaining variables are set up by the variables obtained from an optimization scheme proposed here using a boundary expansion factor of  $f_B = 20$ , which results in an optimized PCE of 24.15 % as shown in Table 3.

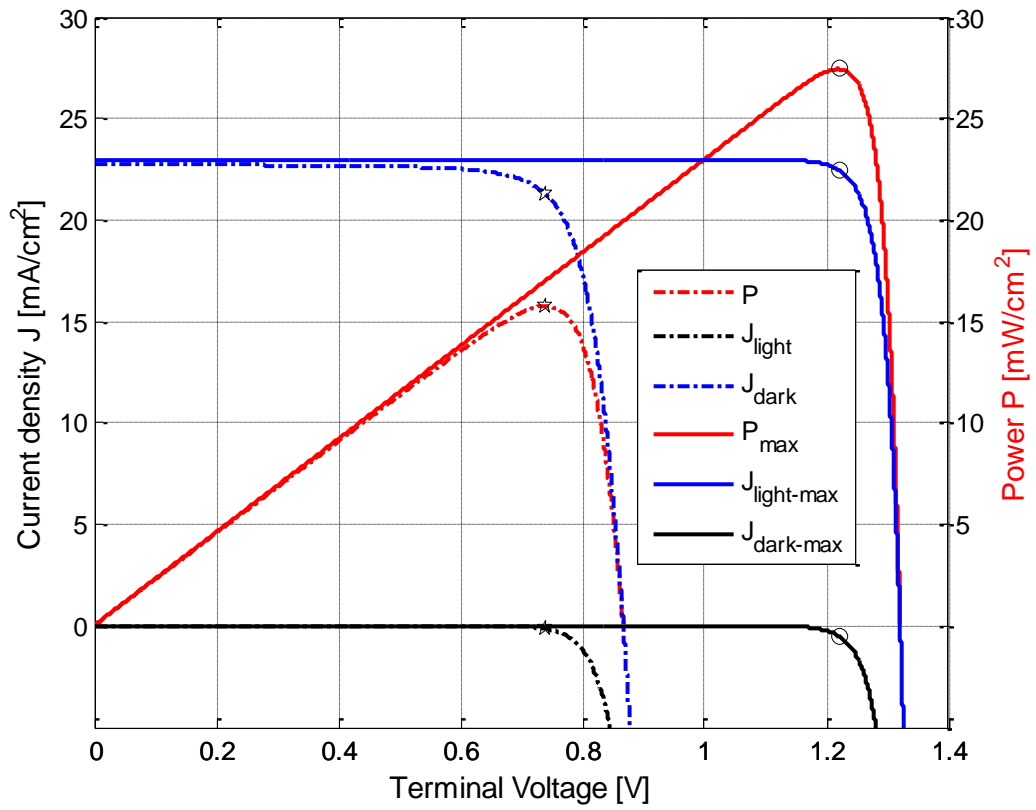


**Figure 3 | Non-optimized and optimized I-V curves, MPP powers and efficiency values.** I-V curves for two different solar cell configurations for the one-dimensional optimization of the model efficiency obtained by Sun et al.<sup>32</sup> and for the multidimensional model optimization obtained in this paper presenting the cell configuration with the maximal obtained efficiency for  $f_B = 160$ : (i) Negative solar cell currents in the dark ( $J_{\text{dark}}$  and  $J_{\text{dark-max}}$ ); (ii) solar cell current under AM 1.5 reference solar irradiance with an irradiance of  $100 \text{ mW/cm}^2$  ( $J_{\text{light}}$  and  $J_{\text{light-max}}$ ); (iii) solar cells power curves ( $P$  and  $P_{\text{max}}$ ). Dashed lines show the modeled curves, which correspond to the measured curves as obtained for the one-dimensional thickness optimization in<sup>32</sup>, and stars show the MPP operation points of these curves with  $\eta_{\text{MPP}} = 15.7 \%$  efficiency. Continuous lines show the values for the presented multidimensional optimization considering  $f_B = 160$  and circles show the MPP operation points of these curves with  $\eta_{\text{MPP-max}} = 27.56 \%$  efficiency.

**Table 1 | Efficiency values obtained for the optimization in one and two-dimensional optimization processes considering different boundary extensions factor  $f_B$  and considering as starting configuration the variable values obtained in Sun et al.<sup>32</sup> leading to the non-optimized initial initial point, with 15.7 % efficiency.**

$f_B = 1.1$										$f_B = 5$									
	$s_f$	$s_b$	$\Delta n$	$\Delta p$	$V_{bi}$	$D_n$	$D_p$	$t_0$	$\lambda_{ave}$		$s_f$	$s_b$	$\Delta n$	$\Delta p$	$V_{bi}$	$D_n$	$D_p$	$t_0$	$\lambda_{ave}$
Sr	16,8	16,8	16,8	16,8	16,8	16,9	16,8	16,8	16,9	Sr	18,3	19,1	18,3	18,3	18,3	18,4	18,8	18,3	18,5
Sb		16,7	16,7	16,7	16,7	16,8	16,7	16,7	16,8	Sb		17,3	17,3	17,3	17,3	18,2	17,3	17,3	17,5
$\Delta n$			16,7	16,7	16,7	16,8	16,7	16,7	16,8	$\Delta n$			17,2	17,2	17,2	17,9	17,3	17,2	17,4
$\Delta p$				16,7	16,7	16,8	16,7	16,7	16,8	$\Delta p$				17,2	17,2	17,9	17,3	17,2	17,4
$V_{bi}$					16,7	16,8	16,7	16,7	16,8	$V_{bi}$					17,2	17,9	17,3	17,2	17,4
$D_n$						16,8	16,8	16,8	16,8	$D_n$						17,9	18,1	17,9	18,1
$D_p$							16,7	16,7	16,8	$D_p$							17,3	17,3	17,4
$t_0$								16,7	16,8	$t_0$								17,2	18,2
$\lambda_{ave}$									16,8	$\lambda_{ave}$									17,4
$f_B = 1.25$										$f_B = 10$									
	$s_f$	$s_b$	$\Delta n$	$\Delta p$	$V_{bi}$	$D_n$	$D_p$	$t_0$	$\lambda_{ave}$		$s_f$	$s_b$	$\Delta n$	$\Delta p$	$V_{bi}$	$D_n$	$D_p$	$t_0$	$\lambda_{ave}$
Sr	17,3	17,3	17,3	17,3	17,3	17,4	17,3	17,3	17,4	Sr	18,4	19,9	18,4	18,4	18,4	18,4	19,4	18,4	18,6
Sb		17,1	17,1	17,1	17,1	17,2	17,1	17,1	17,2	Sb		17,3	17,3	17,3	17,3	18,6	17,3	17,3	17,5
$\Delta n$			17,1	17,1	17,1	17,2	17,1	17,1	17,2	$\Delta n$			17,2	17,2	18,1	17,3	17,3	17,2	17,4
$\Delta p$				17,1	17,1	17,2	17,1	17,1	17,2	$\Delta p$				17,2	17,2	18,1	17,3	17,2	17,4
$V_{bi}$					17,1	17,2	17,1	17,1	17,2	$V_{bi}$					17,2	18,1	17,3	17,2	17,4
$D_n$						17,2	17,2	17,2	17,3	$D_n$						18,1	18,5	18,1	18,3
$D_p$							17,1	17,1	17,2	$D_p$							17,3	17,3	17,5
$t_0$								17,1	17,2	$t_0$								17,2	18,6
$\lambda_{ave}$									17,2	$\lambda_{ave}$									17,4
$f_B = 1.5$										$f_B = 25$									
	$s_f$	$s_b$	$\Delta n$	$\Delta p$	$V_{bi}$	$D_n$	$D_p$	$t_0$	$\lambda_{ave}$		$s_f$	$s_b$	$\Delta n$	$\Delta p$	$V_{bi}$	$D_n$	$D_p$	$t_0$	$\lambda_{ave}$
Sr	17,6	17,7	17,6	17,6	17,6	17,7	17,6	17,6	17,7	Sr	18,4	20,9	18,4	18,4	18,4	18,4	20,1	18,4	18,6
Sb		17,2	17,2	17,2	17,2	17,4	17,2	17,2	17,4	Sb		17,3	17,3	17,3	17,3	19,1	17,3	17,3	17,5
$\Delta n$			17,2	17,2	17,2	17,4	17,2	17,2	17,3	$\Delta n$			17,2	17,2	18,3	17,3	17,2	17,4	
$\Delta p$				17,2	17,2	17,4	17,2	17,2	17,3	$\Delta p$				17,2	18,3	17,3	17,2	17,4	
$V_{bi}$					17,2	17,4	17,2	17,2	17,3	$V_{bi}$					17,2	18,3	17,3	17,2	17,4
$D_n$						17,4	17,4	17,4	17,6	$D_n$						18,3	19,1	18,3	18,5
$D_p$							17,2	17,2	17,4	$D_p$							17,3	17,3	17,5
$t_0$								17,2	17,4	$t_0$								17,2	19,1
$\lambda_{ave}$									17,3	$\lambda_{ave}$									17,4
$f_B = 2$										$f_B = 50$									
	$s_f$	$s_b$	$\Delta n$	$\Delta p$	$V_{bi}$	$D_n$	$D_p$	$t_0$	$\lambda_{ave}$		$s_f$	$s_b$	$\Delta n$	$\Delta p$	$V_{bi}$	$D_n$	$D_p$	$t_0$	$\lambda_{ave}$
Sr	17,8	18,0	17,8	17,8	17,8	18,0	17,9	17,8	18,0	Sr	18,4	21,7	18,4	18,4	18,4	18,3	20,6	18,4	18,6
Sb		17,3	17,3	17,3	17,3	17,6	17,3	17,3	17,4	Sb		17,3	17,3	17,3	17,3	19,5	17,3	17,3	17,5
$\Delta n$			17,2	17,2	17,2	17,5	17,2	17,2	17,4	$\Delta n$			17,2	17,2	18,3	17,3	17,2	17,4	
$\Delta p$				17,2	17,2	17,5	17,2	17,2	17,4	$\Delta p$				17,2	17,2	18,3	17,3	17,2	17,4
$V_{bi}$					17,2	17,5	17,2	17,2	17,4	$V_{bi}$					17,2	18,3	17,3	17,2	17,4
$D_n$						17,5	17,6	17,5	17,7	$D_n$						18,3	19,5	18,3	18,5
$D_p$							17,2	17,2	17,4	$D_p$							17,3	17,3	17,5
$t_0$								17,2	17,6	$t_0$								17,2	19,5
$\lambda_{ave}$									17,4	$\lambda_{ave}$									17,4
$f_B = 2.5$										$f_B = 100$									
	$s_f$	$s_b$	$\Delta n$	$\Delta p$	$V_{bi}$	$D_n$	$D_p$	$t_0$	$\lambda_{ave}$		$s_f$	$s_b$	$\Delta n$	$\Delta p$	$V_{bi}$	$D_n$	$D_p$	$t_0$	$\lambda_{ave}$
Sr	18,0	18,3	18,0	18,0	18,0	18,2	18,2	18,0	18,2	Sr	18,4	22,5	18,4	18,4	18,4	18,4	21,0	18,4	18,6
Sb		17,3	17,3	17,3	17,3	17,8	17,3	17,3	17,5	Sb		17,3	17,3	17,3	17,3	19,9	17,3	17,3	17,5
$\Delta n$			17,2	17,2	17,2	17,6	17,3	17,2	17,4	$\Delta n$			17,2	17,2	17,2	18,4	17,3	17,2	17,4
$\Delta p$				17,2	17,2	17,6	17,3	17,2	17,4	$\Delta p$				17,2	17,2	18,4	17,3	17,2	17,4
$V_{bi}$					17,2	17,6	17,3	17,2	17,4	$V_{bi}$					17,2	18,4	17,3	17,2	17,4
$D_n$						17,6	17,7	17,6	17,8	$D_n$						18,4	19,9	18,4	18,6
$D_p$							17,3	17,3	17,4	$D_p$							17,3	17,3	17,5
$t_0$								17,2	17,8	$t_0$								17,2	19,9
$\lambda_{ave}$									17,4	$\lambda_{ave}$									17,4

$s_f$ , surface recombination velocity of the front charge conduction layer;  $s_b$ , surface recombination velocity of the back charge conduction layer;  $\Delta n$ , number of excess electrons per unit volume that are available for the recombination process within the p-type layer;  $\Delta p$ , number of excess holes per unit volume that are available for the recombination process within the n-type layer;  $V_{bi}$ , built-in voltage;  $D_n$ , diffusion coefficients of electrons;  $D_p$ , diffusion coefficient of holes;  $t_0$ , absorber layer thickness;  $\lambda_{ave}$ , average optical decay length.

**Table 2 | Optimization data related to the nine dimensional optimization by use of the maximal boundary extensions of the model variables, setting up the boundary extension factor to  $f_B = 160$ .**

Variable specification	$S_f$	$S_b$	$\Delta n$	$\Delta p$	$V_{bi}$	$D_n$	$D_p$	$t_0$	$\lambda_{ave}$	$\eta$
Units	[ cm / s ]	[ cm / s ]	[ 1 / cm <sup>3</sup> ]	[ 1 / cm <sup>3</sup> ]	[ V ]	[ cm <sup>2</sup> / s ]	[ cm <sup>2</sup> / s ]	[ nm ]	[ nm ]	[ % ]
1 - Values obtained in (Sun et al.,2015) <sup>32</sup>	2,00E+02	1,92E+01	8,43E+06	1,30E+08	0,78	5,00E-02	5,00E-02	450,0	100,0	15,7
2 - Lower boundary values	1,25E+00	1,20E-01	5,27E+04	8,13E+05	0,00	3,13E-04	3,13E-04	2,81	0,63	-
3 - Lower boundary modification	1 / 160	1 / 160	1 / 160	1 / 160	1 / 8	1 / 160	1 / 160	1 / 160	1 / 160	-
4 - Upper boundary values	3,20E+04	3,07E+03	1,35E+09	2,08E+10	1,40	8,00	8,00	7,20E+04	1,60E+04	-
5 - Upper boundary modification	160	160	160	160	1,89	160	160	160	160	-
6 - Optimized values	1,25	0,12	8,43E+06	1,30E+08	1,40	8,00	8,00	5,17	0,63	27,56
7 - Modification factors of the optimization	1 / 160	1 / 160	n. m.	n.m.	1,8	160,0	160	1 / 87	1 / 160	-

Line 1, Cell properties and manufacturing parameters obtained from the one-dimensional thickness optimization in Sun et al.<sup>32</sup>, which represent the initial conditions;  
Line 2 The constraining lower boundary limits specified for the optimization and the related boundary modification (Line 3);  
Line 4, The constraining upper boundary limits specified for the optimization and the related boundary modification (Line 5);  
Line 6, The ideal model variable values obtained from the multidimensional optimization process;  
Line 7, The actual modification factors calculated with the values from Line 6. (n.m., not modified)

**Table 3 | Optimized model variables in nine dimensional optimizations as function of several boundary extension factors  $f_B$ .**

$f_B$	$S_f$	$S_b$	$\Delta n$	$\Delta p$	$V_{bi}$	$D_n$	$D_p$	$t_0$	$\lambda_{ave}$	$\eta$
[ - ]	[ cm / s ]	[ cm / s ]	[ 1 / cm <sup>3</sup> ]	[ 1 / cm <sup>3</sup> ]	[ V ]	[ cm <sup>2</sup> / s ]	[ cm <sup>2</sup> / s ]	[ nm ]	[ nm ]	[ % ]
<b>1,10</b>	181,82	17,45	8,43E+06	1,30E+08	0,86	0,06	0,06	409,09	90,91	16,97
<b>1,25</b>	160,00	15,36	8,43E+06	1,30E+08	0,98	0,06	0,06	386,22	80,00	17,64
<b>1,50</b>	133,33	12,80	8,43E+06	1,30E+08	1,17	0,08	0,08	337,14	66,67	18,15
<b>2,00</b>	100,00	9,60	8,43E+06	1,30E+08	1,40	0,10	0,10	257,69	50,00	18,83
<b>5,00</b>	40,00	3,84	8,43E+06	1,30E+08	1,40	0,25	0,25	105,79	20,00	20,94
<b>10,00</b>	20,00	1,92	8,43E+06	1,30E+08	1,40	0,50	0,50	53,76	10,00	22,54
<b>20,00</b>	10,00	0,96	8,43E+06	1,30E+08	1,40	1,00	1,00	27,27	5,00	24,15
<b>30,00</b>	6,67	0,64	8,43E+06	1,30E+08	1,40	1,50	1,50	18,33	3,33	25,09
<b>40,00</b>	5,00	0,48	8,43E+06	1,30E+08	1,40	2,00	2,00	13,83	2,50	25,76
<b>60,00</b>	3,33	0,32	8,43E+06	1,30E+08	1,40	3,00	3,00	9,28	1,67	26,70
<b>80,00</b>	2,50	0,24	8,43E+06	1,30E+08	1,40	4,00	4,00	7,95	1,25	27,25
<b>100,00</b>	2,00	0,19	8,43E+06	1,30E+08	1,40	5,00	5,00	7,25	1,00	27,44
<b>120,00</b>	1,67	0,16	8,43E+06	1,30E+08	1,40	6,00	6,00	6,65	0,83	27,52
<b>140,00</b>	1,43	0,14	8,43E+06	1,30E+08	1,40	7,00	7,00	6,14	0,71	27,55
<b>160,00</b>	1,25	0,12	8,43E+06	1,30E+08	1,40	8,00	8,00	5,71	0,63	27,56

## Supplementary information

### Maximum efficiency of perovskite solar cells by material properties tuning and cell design: a multidimensional approach

Manfred Georg Kratzenberg<sup>1,2\*</sup>, Ricardo R  ther<sup>2</sup> & Carlos Renato Rambo<sup>1</sup>

<sup>1</sup> Electrical Materials Laboratory (LAMATE), Department of Electrical Engineering , Universidade Federal de Santa Catarina (UFSC), Trindade, PO Box 476, 88040-970 Florian  polis, Santa Catarina (SC), Brazil,

<sup>2</sup> Fotovoltaica UFSC – Solar Energy Research Laboratory, Department of Civil Engineering, Universidade Federal de Santa Catarina (UFSC), Av. Luiz Boiteux Piazza, 1302, Florian  polis, SC, Brazil.

This file includes the following supplementary information (SI): Supplementary presentation of the model; basic differential equations from which the model was derived; supplementary discussions and supplementary manufacturing recommendations (SI-1 – SI-5):

SI-1. Analytical model of the perovskite pin-type solar cells

SI-1.1. Two I-V curve models

SI-1.2. Analytical model for the determination of the recombination currents

SI-1.3. Analytical model for the determination of the photocurrent

SI-1.4 Fundamental equations from which the analytical model was derived and detailed optimization setup

SI-2. Most sensible model variables

SI-3. Contribution of each variable under variation of the boundary conditions in multidimensional optimizations and effects of the absorber layer thickness

SI-4. Manufacturing recommendations for efficiency enhancement

SI-4.1. Effective front and back surface recombination velocities

SI-4.2. Diffusion coefficients of electrons and holes

SI-4.3. Average optical decay length

SI-4.4. Absorber layer thickness

SI-4.5. Built-in voltage

SI-4.6. Quantity of excess holes and electrons

SI-4.7 Nomenclatures, Indexes, and References for Supplementary information.

## **SI-1. Analytical model of the perovskite pin-type solar cells**

This section provides the detailed understanding of the charge generation and recombination processes within a perovskite solar cell. Sun et al.<sup>32</sup> elaborated a simplified analytical model for four different types of perovskite solar cell devices considering a fixed band gap, where the highest efficiency was obtained with an absorber layer thickness optimized pin-type device, which presented a measured efficiency of 15.7 %<sup>32</sup>. As this analytical model uses some general simplifications, the authors validated its accuracy by comparison of the modeled and the measured efficiency of a manufactured solar cell, which presented a low dissimilarity of only 0.1 %. In the present multidimensional optimizations only the highest efficiency pin-type analytical model was used, whose I-V curves, measured in the dark and under reference illumination, present a nearly perfect superposition with the modeled curves<sup>32</sup>. This analytical model and the values of its model variables are used here as initial conditions for the optimization of the PCE in a multidimensional variable space of material properties and the absorber layer thickness. For simplicity of the modeling, only a fixed band gap and the configuration of valence and conduction bands of the electrodes, charge conduction layers and the absorption layer, as specified in Figure 1a, were considered. Specific range restrictions define ranges at which the values of the variables can vary during an optimization. These range restrictions are expressed by different amplification factors  $f_b$  in different optimizations. The analytical model is based on a self-consistent stationary quantum simulation of the charge carrier generation, which was raised up by derivations of the drift-diffusion and the Poisson equations<sup>32</sup>. This analytical model is a simplified version of the numerical model of the charge carrier generation, which can also be derived from the drift-diffusion and the Poisson equations<sup>35-38</sup>. With both the analytical and the numerical model, the total generation of charges is obtained by the integration of the locally-generated charges over the whole absorber layer thickness. Whereas the numerical model simulates in



a very detailed form the charge carrier generation as function of the solar radiation wavelength, the present analytical model stands out because of its good approximation and its relatively low computational cost, which allows its use in a large number of numerical optimizations, in exhaustive random optimizations, or in further analyses, which are also based on large sets of necessary model simulations.

### SI-1.1. The two I-V curve models

In a manufactured solar cell two different I-V curves can be measured: (i) the curve when the cell is exposed to a reference light source  $J_{\text{light}}(G, V)$ ; and (ii) the curve when it is in the complete dark  $J_{\text{dark}}(V)$  (Figure 3). By the superposition of these two measured curves, the curve of the intern photo-generated current density  $J_{\text{photo}}(G, V)$ , in units of  $[A/cm^3]$ , can be specified. This current density only considers radiative recombination losses and can be calculated by equation (S1)<sup>32</sup>.

$$J_{\text{photo}}(G, V) = J_{\text{light}}(G, V) - J_{\text{dark}}(V) \quad (\text{S1})$$

In this equation,  $G [s^{-1}cm^{-2}]$  is the charge generation rate per solar cell area, and  $V$  is the externaterminal voltage of the solar cell. This superposition considers an equal short-circuit current density  $J_{\text{photo}}(G, V) = J_{\text{light}}(G, V)$ , at  $V = 0$ , while for the remaining curve points, the intern photocurrent density is larger than the measurable current density  $J_{\text{light}}$  ( $J_{\text{photo}}(G, V) > J_{\text{light}}(G, V)$ ). This leads to a higher open circuit voltage of the non-measurable photocurrent ( $V_{\text{oc-photo}}$ ) in comparison to the solar cell's open circuit voltage ( $V_{\text{oc-light}} = V_{\text{oc}}$ ). This measurable open circuit voltage is reduced by reason of the non-radiative recombination effects, which are modeled by use of the measured I-V curve when the cell is kept in the dark ( $J_{\text{dark}}$ ), a simplification which can be adopted, considering the superposition principle<sup>32</sup>. As the present model is a simplification of the PSC, it depreciates some very small parts of

the radiation, which are: (i) the absorption of solar radiation within the charge conduction layers and the back reflector; (ii) the light emitted by the solar cell's top surface, where one part is due to front surface reflection; and the other part is light, which comes from the cell's back reflector and is not absorbed within the cell. Furthermore, the transmission losses of the cell's front glass cover are also depreciated by this model. Such losses are present in a manufactured solar cell but do not appear in the mathematical model of the PSC considered here. Therefore, it has to be remembered that the measured short-circuit current  $J_{sc-med}(G, V=0)$ , is to some minute extent smaller than the theoretically maximal attainable short-circuit current  $J_{sc-mod}$  as expressed in the present model (equation S2).

$$J_{sc-med}(G, V=0) < J_{sc-mod} = q G_{max} \quad (S2)$$

Where  $q = -1.6021765 \times 10^{-22}$  [mAs] is the electric charge energy of an electron or a hole and  $G_{max}$  [ $s^{-1} m^{-2}$ ] is the maximal attainable charge carrier generation, for a specific band gap of the solar cell, wherein the present cell  $q G_{max}$  is 23 mA/cm<sup>2</sup> as obtained by the optical transfer matrix method<sup>32</sup>. Considering the superposition in equation (S1), the total cell current density under light exposure (Figure 3 -  $J_{light}$ ) can be modeled by equation (S3)<sup>32</sup>, with the sum of: (i) the measurable current density in the dark (equation S5), which express the recombination current density and has a negative sign (Figure 3 -  $J_{dark}$ ); and (ii) current density which is generated by the photons ( $J_{photo}$ ) (equation S14), having a positive sign, and which is not visible in Figure 3.

$$J_{light}(G, V) = J_{dark}(V) + J_{photo}(G, V) \quad (S3)$$

Both the photocurrent density and the current density in the dark are comprised of its electron and hole current densities, which results in the following expression for the total current density of charge carriers.

$$J_{tot} = J_{light} = J_{n-photo} + J_{p-photo} + J_{n-dark} + J_{p-dark} = J_n + J_p \quad (S4)$$

Where each one of the currents  $J_n$  and  $J_p$  does present one part, which interprets the injection of generated charge carriers ( $J_{n\text{-photo}}$ ,  $J_{p\text{-photo}}$ ) by the solar irradiance and a further part which stands for the recombination of the generated charge carriers ( $J_{n\text{-dark}}$ ,  $J_{p\text{-dark}}$ ).

### SI-1.2. Analytical model for the determination of the recombination currents

In this model, a total of six types of different recombination effects are accounted for: (i) electrons, which casually pass the hole conduction and electron blocking layer; (ii) holes, which eventually pass the electron conduction and hole blocking layer; (iii) charge carriers, which escape at the wrong contact; (vi) recombination due to interface defects at the transition between arbitrary perovskite crystals within the absorber layer; (v) recombination due to interface defects at the transition between the absorber layer and the transport layers of charge carriers; and finally (vi) recombination within the bulk of the p and n charge transport layers, which may appear e.g. due to pinholes in these layers, and which thus decrease the shunt resistance of the PSC<sup>51</sup>. The exponential behavior of the I-V curve in the dark  $J_{\text{dark}}$  [mA/cm<sup>2</sup>] presents the PSC current density if a variable external voltage  $V$  is applied to the cell's terminals in the absence of light and can be modeled as follows.

$$J_{\text{dark}} = (\alpha_f J_{f0} + \alpha_b J_{b0}) (e^{V/V_t} - 1) \quad (\text{S5})$$

Where  $J_{f0}$  [mA/cm<sup>2</sup>] and  $J_{b0}$  [mA/cm<sup>2</sup>] are the current densities of the recombination current\* in the front and back charge conduction layers, which are calculated by equations (S6) and

---

\* In heterojunction solar cells a large number of recombination centers appear, as a consequence of the anisotropic crystal structure at the termination of the semiconductors crystals involved, due to the use of distinct materials for the n-type, the p-type and the i-type layers. These effects lead to recombination effects at the front and back transition surfaces of the perovskite absorber layer and lead therefore, to a significant impact on the behavior of semiconductor devices. The dangling bonds at these transition surfaces introduce a large number of electrically active states, which result in higher defect densities, leading therefore, to a reduction of the open-circuit voltage  $V_{OC}$  and the maximal power point voltages  $V_{MPP}$ <sup>52</sup>. Furthermore, these transition surfaces tend to contain more impurities and defects, which are acquired e.g. in silicon solar cells during the fabrication process, when devices are exposed to air and humidity<sup>50</sup>. Electronically active states for holes and electrons can additionally be present between single perovskite crystals within the absorber layer. Another recombination effect related to the transition between the charge conduction layers and the absorber layer occurs by reason of holes, which present a lower energy, and electrons, which present a higher energy than the

(S7). The dimensionless scaling coefficients of these recombination currents,  $\alpha_f$  and  $\alpha_b$  are calculated by use of equations (S8) and (S9). The variable  $V$  in equation (S5) is the variable terminal voltage of the solar cell and  $V_t$  [V] is the thermal voltage, which is calculated by  $V_t = k_B T / q$ , where  $k_B = 1.38064852 \times 10^{-23}$  [J/K] is the Boltzmann constant;  $q = 1.60217662 \times 10^{-19}$  [As] is the elementary charge, which determines the energy of an electron or hole; and  $T$  [K] is the operation temperature of the solar cell at the moment when the two I-V curves are measured. The recombination current of electrons ( $J_{f0}$ ) at the front hole conduction and electron-blocking layer (HC-EBL) appears by reason of the parasitic conduction of electrons, which have a higher energy than the potential of the blocking barrier of the HC-EBL (Fig. 1a). Conversely, the recombination current of holes ( $J_{b0}$ ) at the back electron conduction and hole blocking layer (EC-HBL) appears by reason of a parasitic conduction of holes, which have a lower energy than the blocking potential of the EC-HBL (Fig. 1a). The second reason for recombination of electrons occurs by reason of an occasional trapping of electrons as a consequence of positive trapping states at the perovskite crystal termination. This effect appears especially in non-passivated absorber layers and the order of magnitude higher electron recombination current  $J_f$ , as in comparison to the hole recombination current  $J_b^*$  (Table 2, line 1) may possibly be present by reason of these positive trap states. The recombination current densities are calculated in a PSC as follows:

$$|J_f| = J_{f0} = q s_f \Delta n = q s_f (n - n_0) \quad (S6)$$

$$|J_b| = J_{b0} = q s_b \Delta p = q s_b (p - p_0) \quad (S7)$$

---

blocking barriers designed by the charge conduction and blocking layers in a PSC (Fig. 1a), which lead also to the recombination currents  $J_f$  and  $J_b$ .

\* In PSC the loss of iodine at the perovskite  $\text{CH}_3\text{NH}_3\text{PbI}_{3-x}\text{Cl}_x$  crystal termination or crystal surface leads to vacancy sites, resulting in a local positive charge attached to the Pb atom. This local inhomogeneity of the crystal structure, therefore, represents a coulomb trap of electrons, also called a trap state<sup>68</sup>.

By assumption of the superposition principle<sup>32</sup>, it is considered that the two recombination currents in the dark ( $J_{f0}$ ,  $J_{b0}$ ), are equal to the recombination currents under exposure to light ( $J_f$ ,  $J_b$ ), meaning that  $|J_f| = J_{f0}$  and  $|J_b| = J_{b0}$ . This principle considers also that the cell's recombination losses under its exposure to light are expressed by the I-V curve behavior in the dark, which is defined by equation (S5). In equation (S6) the variable  $\Delta n$  [ $\text{cm}^{-3}$ ] presents the number of excess electrons per unit volume that are available for the recombination process within the p-type layer. This excess number of electrons occurs if the actual number of electrons ( $n$ ) in this layer is higher than the number of electrons under thermal equilibrium condition ( $n_0$ )<sup>\*</sup>, where  $\Delta n = n - n_0$ . Conversely  $\Delta p$  [ $\text{cm}^{-3}$ ] in equation (S7) is the number of excess holes per unit volume that are available to recombine within the n-type semiconductor, which occurs if the actual number of holes within this p-type layer is higher than the number of holes in thermal equilibrium  $p_0$ , where  $\Delta p = p - p_0$ . The effective surface recombination velocity  $s_f$  [ $\text{cm/s}$ ] in equation (S6) represents the effective velocity or rate at which the minority electrons within the intrinsic layer recombine at the surface transition to the hole conduction layer. In contrast,  $s_b$  [ $\text{cm/s}$ ] is the effective velocity or rate at which the minority holes from the absorber layer recombine at the interface between the electron conduction layer and the absorber layer. As the units of  $s_f$  and  $s_b$  are [ $\text{cm/s}$ ], they can also be thought as the effective speeds at which electrons and holes move toward dangling bond positive and negative trap states at the perovskite crystal surface<sup>†</sup>. The dimensionless coefficients  $\alpha_f$  and  $\alpha_b$  in equation (S5) are used in order to reduce the large analytical expressions obtained from the derivation process of the analytical PSC model. They can be

---

\* Thermal equilibrium of a semiconductor is a state where no external energy is added to this semiconductor due to irradiation, voltage or temperature.

† PV-Education, Surface Recombination velocity, <http://www.pveducation.org/pvcdrom/surface-recombination>.

considered as scaling coefficients of the front and back components of the recombination currents, which are calculated as follows.

$$\alpha_f = \frac{1}{\frac{e^{V'} - 1}{V'} + \beta_f} \quad (\text{S8})$$

$$\alpha_b = \frac{1}{\frac{e^{V'} - 1}{V'} + \beta_b} \quad (\text{S9})$$

Where the dimensionless coefficients  $\beta_f$  and  $\beta_b$ , used in (S8) and (S9), are calculated by equations (S12) and (S13). The variable  $V'$  translates the resultant electric field in a dimensionless form and is determined as follows.

$$V' = (V - V_{bi}) / V_t \quad (\text{S10})$$

Where  $V_t = k_B T / q$  [V] is the thermal voltage;  $V_{bi}$  [V] is the device's built-in voltage and  $V$  [V] is its terminal voltage and  $T$  [K] is its assumed operation temperature. The terminal voltage  $V$  is an imposed and measurable voltage, which varies in the range  $0 \dots V_{0c}$ , where  $V_{0c}$  [V] is the cell's open circuit voltage. In the dark, the terminal voltage has to be imposed to the solar cell's electrodes by an external variable voltage supply. The built-in voltage ( $V_{bi}$ ) is calculated by equation (S11) and can be manipulated by material selection of the charge conduction layers. Alternatively,  $V_{bi}$  can also be modified via additional doping of the selected charge conduction layers. Both manipulations result in the adjustment of the band

gap energy of the transport layers<sup>\*</sup>. The built-in voltage of the pin-type cell is calculated as follows.

$$V_{bi} = V_t \log \left( \frac{N_{A,eff} N_{D,eff}}{n_i^2} \right) \quad (S11)$$

Where  $N_{D,eff}$  [1/cm<sup>3</sup>] is the effective doping concentration of the donor molecules, which are able to donate additional electrons that are fixed into the crystal lattice of the n-type charge conduction layer, while  $N_{A,eff}$  [1/cm<sup>3</sup>] is the effective doping concentration of acceptor molecules, which are able to accept electrons that are fixed into the crystal lattice of the p-type charge conduction layer. The intrinsic carrier density  $n_i$  [1/cm<sup>3</sup>] in equation (S11) is the inherent carrier density to the undoped p and n-type layers, and it is considered to be very small. In silicon solar cells the intrinsic carrier density is equal in both charge conduction layers. The dimensionless coefficients  $\beta_f$  and  $\beta_b$  in equations (S8) and (S9) determine mainly the PSC's Fill Factor<sup>32</sup> and are calculated with the following equations for the front and the back charge transport layers respectively.

$$\beta_f = D_n / (t_0 S_f) \quad (S12)$$

$$\beta_b = D_p / (t_0 S_b) \quad (S13)$$

In equations (S12) and (S13)  $t_0$  is the thickness of the intrinsic absorber layer and  $D_p$  and  $D_n$ , both measured in units of [cm<sup>2</sup>/s], are the diffusion coefficients of holes and electrons.

From the discussions resulting in equations (S5) to (S13), it can be seen that the recombination current in the dark ( $J_{dark}$ ) of this solar cell is a function of the whole set of model variables of the PSC, excluding the average optical decay length. These variables are:

---

<sup>\*</sup> As the energy potentials and band gaps of the organic charge conduction layers have to be adjusted in accordance to the configured band gap of the perovskite absorber layer (Figure 1a), a correct matching of the band gap of these layers also increases the built-in voltage<sup>32</sup>.

the effective surface recombination velocity of electrons ( $s_b$ ) [m/s], mainly occurring at the surface of the front hole conduction layer; the effective surface recombination velocity of holes ( $s_f$ ) [m/s], principally present at the surface of the back hole conduction layer; the number of excess electrons available for the recombination process  $\Delta n$  [cm<sup>-3</sup>]; the number of excess holes that can participate at recombination process  $\Delta p$  [cm<sup>-3</sup>]; the diffusion coefficient of electrons  $D_n$ , which specify the diffusion of electrons in random directions; the diffusion coefficient of holes  $D_p$ , which specify the diffusion of holes in random directions [cm<sup>2</sup>/s]; the solar cell's built-in voltage  $V_{bi}$  [V]; the absorber layer thickness  $t_0$  [nm], the cells temperature (T) [K]; and the terminal voltage  $V$  [V].

### SI-1.3. Analytical model for the determination of the photocurrent

Under light exposure of the solar cell, the photogeneration current  $J_{photo}(G,V)$  can be expressed by the following equation.

$$J_{photo}(G, V) = q G_{max} (A - B e^{-m}) \quad (S14)$$

Where A and B are dimensionless parameters, which are used in order to replace some larger terms as given by equations (S15) and (S16), and were obtained by the derivation of this analytical solar cell model<sup>32</sup>

$$A = \alpha_f \left( \frac{1 - e^{V' - m}}{V' - m} - \beta_f \right) \quad (S15)$$

$$B = \alpha_b \left( \frac{1 - e^{V' + m}}{V' + m} - \beta_b \right) \quad (S16)$$



In equations (S15) and (S16) the following dimensionless coefficients were calculated: (i)  $\alpha_f$  and  $\alpha_b$  by use of equations (S8) and (S9); (ii)  $V'$  by use of equation (S10); and (iii)  $\beta_f$  and  $\beta_b$  by use of equation (S12) and (S13). The dimensionless ratio ( $m$ ) relates in equation (S17) the average optical decay length ( $\lambda_{ave}$ ) and the absorber thickness  $t_0$ , both measured in [nm].

$$m = t_0 / \lambda_{ave} \quad (S17)$$

The generation of charges  $G(x)$  [ $s^{-1}cm^{-2}$ ], appearing in equations (S1) and (S2) and (S14), is calculated by equation (S18), and is a function of the photon penetration depth  $x$  in the absorber layer, where  $x = 0 \dots t_0$ . The true charge generation curve in a solar cell has an oscillating decay, as specified by the superposition of the solar radiation waves in top-down and bottom-up directions, where the photon flux in the bottom-up, or the backward direction, is the reflected photon flux at the back reflector and the layer interfaces. This effect occurs by means of the superposition of light waves which are not in phase, and it can be modeled by the use of the optical transfer matrix method as cited in Sun et al.<sup>32</sup>. However, in a simplification, this decay curve can also be modeled by the adoption of an exponential decay as specified by the Beer-Lambert law, where each wavelength has a specific optical decay length. In a second simplification, this exponential decay is given for the average optical decay length (equation S18), which is the average of the optical decay lengths of the involved wavelengths.

$$G(x) = G_{eff} e^{-x / \lambda_{ave}} \quad (S18)$$

In this simplification the average of a complete set of wavelength-dependent optical decay lengths ( $\lambda_y = \lambda_{min} \dots \lambda_{max}$ ), also sometimes referred to as the optical absorption lengths, leads in the present model to an approximation which is specified as average optical decay length ( $\lambda_{ave}$ ).  $G_{eff}$  [ $s^{-1}cm^{-2}$ ] is the effective generation of charge carriers, which is equal to the

highest charge generation at the top of the absorber layer at  $x = 0$ . Both  $\lambda_{ave}$  and  $G_{eff}$  are specific constants related to the absorber layer, where each of these constants is an average value, considering the absorption and generation related to the wavelengths of the whole solar spectrum. Where  $\lambda_{ave}$  can be improved by light trapping effects or absorber layer material selection  $G_{eff}$  can be improved by the band gap tunings of the considered solar cell. In order to understand equation (S18) better, the charge generation characteristic of this equation is visualized for a set of different  $\lambda_{ave}$  in Fig. 1b. The range of the charge generation  $G(x)$  is normalized in this figure and the value of  $G_{eff}$  corresponds, therefore, to 100%. At zero penetration depth ( $x = 0$ ), the penetration dependent charge generation  $G(x)$  is equal to the effective charge generation ( $G(x) = G_{eff}$ ), and  $G(x)$  decays exponentially as a function of the penetration depth. This behavior is consistent with the number of available photons, which decays exponentially as a function of the solar radiation penetration depth reaching at  $\lambda_{ave}$  a value of  $0.36 G_{eff}$  in the exponential curves in Figure 1b. The sum of the photons which are converted to free charges within the absorber layer ( $G_{max}$ ) is given by the integration of the generated charges  $G(x)$  over the absorber layer thickness at the depths  $x = 0 \dots t_0$ . The correct dimension of the absorber layer thickness  $G_{max}$  determines the maximum absorption of photons  $G_{max} [s^{-1}cm^{-2}]$  by equation (S19), and if the absorber layer is too thin, a significant number of photons might not be absorbed and converted by the absorber layer as can be directly visualized by Figure 1b. In this equation,  $G_{max}$  is obtained by the integration of  $G(x)$  over the whole absorber layer thickness  $t_0$  [nm] as follows.

$$G_{max} = \int_{x=0}^{t_0} G(x) dx = \int_{x=0}^{t_0} G_{eff} e^{-x/\lambda_{ave}} dx \quad (S19)$$

In an approximation, which considers ( $t_0 = \infty$ ) the integration of equation (S19) results in the following equation.

$$G_{\max} = G_{\text{eff}} \lambda_{\text{ave}} \quad (\text{S20})$$

Such a simplification leads to a small uncertainty as it adds mathematically a minute part of the solar radiation, the part from  $t_0$  to infinity in the Beer-Lambert curve (not visible in Fig. 1b), which is not supposed to be present in a manufactured PSC. Considering the cell configuration as used by Sun et al.<sup>32</sup>, with  $\lambda_{\text{ave}} = 100$  nm, the radiation part related to ( $x = t_0 \dots \infty$ ) is only 1 %, as seen from its value of  $(0.01 G_{\text{eff}})$  for  $t_0 = 450$  nm in Fig. 1b. However, the most radiation of this remaining 1 % is reflected by the back reflector contact, and therefore, the major portion of this back reflected part indeed generates free charges, which is in agreement with the proposed model. Thus, some minute fractions, which are considered by the model and are not present in a manufactured PSC, are: (i) the small portion of solar radiation, which is absorbed by the back reflector; and (ii) the part of the back reflected radiation, which is not converted into free charges and is consequently emitted by the solar cell's front surface. Due to these model simplifications, Sun et al.<sup>32</sup> obtained a small dissimilarity with an absolute error of 0.1 % between the modeled and measured PCE values. From the discussions resulting in equations (S14) to (S20), the modeling of the internal and not measurable photocurrent is obtained as a function of the same model variables as specified for calculating the solar cell current in the dark. Additionally the average optical decay length  $\lambda_{\text{ave}}$  [nm], which defines the effective optical thickness of the absorber layer, as well as the effective generation of charge carriers  $G_{\text{eff}}$ , which is proportional to the number of generated charge carriers considering the cells band gap, are included in the model in order to simulate the current shape of the photocurrent.

#### SI-1.4 Fundamental equations from which the analytical model was derived and detailed optimization setup

The present model as derived in Sun et al.<sup>32</sup> is based on the solutions of a total of five second-order differential equations involving a total of ten integration constants. The assumed simplifications in this model result in limited uncertainties as validated by numerical simulations and measurements with a manufactured solar cell in Sun et al.<sup>32</sup>. The first differential equation is the second-order Poisson differential equation which defines the relationship between the space charge and the electric field as follows:

$$\frac{\partial^2 \phi(x)}{\partial x^2} = -\frac{\rho}{\varepsilon} = -\frac{\rho}{\varepsilon_r \varepsilon_0} = 0 \quad ; \quad \rho = 0 \quad (\text{S21})$$

Where  $\phi(x)$  is the electrostatic potential at a specific penetration depth  $x$  of the solar irradiance in the absorber layer;  $\rho$  [ $\text{m}^{-3}$ ] is the density of charge carriers and  $\varepsilon$  [F/m] is the absolute permittivity of the intrinsic layer, which is the product of the relative permittivity  $\varepsilon_r$  and the vacuum permittivity  $\varepsilon_0$ . As the intrinsic absorber i-type layer is undoped, its density of charges  $\rho$  is equal to zero ( $\rho = 0$ ). Considering this detail, the integration of the Poisson equation results in the following general solution

$$\phi(x) = C_1 x + C_2 \quad (\text{S22})$$

Where  $C_1$  and  $C_2$  are arbitrary integration constants. The exact solution of this equation is obtained by consideration of two boundary conditions<sup>32</sup>. The first boundary condition is given for zero penetration of the solar irradiance in the absorber layer ( $x = 0$ ), where the electrostatic potential is defined as follows:

$$\phi(x = 0) = \phi(0) = 0 \quad (\text{S23})$$

The second boundary condition is specified for the maximal penetration depth of the solar irradiance in the absorber layer, where the electrostatic potential is given as follows:

$$\phi(x = t_0) = \phi(t_0) = (V_{bi} - V) \quad (S24)$$

Substituting separately these two Dirichlet boundary conditions in the general solution of the Poisson equation (S22), and solving the obtained system of two equations, results in the following specific solution for the electrostatic potential  $\phi(x)$  [V]:

$$\phi(x) = -\frac{(V - V_{bi})}{t_0} x = -E x \quad (S25)$$

Where the built-in voltage ( $V_{bi}$ ), is specified by equation (S11). Solving equation (S25) for  $E$  results in the equation of the built-in electric field  $E$  [V/m] as follows:

$$E = (V - V_{bi}) / t_0 \quad (S26)$$

This electric field equation is used to calculate the charge carrier generation in a PSC by its substitution in the Schrödinger drift-diffusion model, which defines the charge transport of electrons and holes considering a self-consistent stationary quantum simulation. The self-consistent stationary quantum simulation defines that there is no variation in the density of electrons and holes over time ( $\partial n / \partial t = 0$ ,  $\partial p / \partial t = 0$ ). With this consideration, the continuity equations of a perovskite solar cell under light exposure are defined by equations (S27) and (S28).

$$\frac{\partial n}{\partial t} = 0 = \frac{1}{q} \frac{\partial J_n}{\partial x} + G(x) - R(x) \quad (S27)$$

$$\frac{\partial p}{\partial t} = 0 = -\frac{1}{q} \frac{\partial J_p}{\partial x} + G(x) - R(x) \quad (S28)$$

Where  $J_n$  and  $J_p$  are the generated current densities of electrons and holes, which are

specified by the differential equations of the current densities in (S29) and (S30).  $G(x)$  and  $R(x)$  are the penetration depth specific photogeneration and recombination rates of charge carriers.

$$J_n = q \mu_n n E + q D_n \frac{\partial n}{\partial x} \quad (\text{S29})$$

$$J_p = q \mu_p p E + q D_p \frac{\partial p}{\partial x} \quad (\text{S30})$$

In the current density equations (S29) and (S30), the first terms on the right side describe the drift component of electrons and holes, while the second term translates the diffusion component. Substituting  $J_n$  in equation (S27) with the expression in (S29) and substituting  $J_p$  in (S28) with the expression in (S30) results in the Schrödinger drift-diffusion equations of electrons and holes as specified in (S31) and (S32).

$$D_n \frac{\partial^2 n(x)}{\partial x^2} + \mu_n E(x) \frac{\partial n(x)}{\partial x} + G(x) - R(x) = 0 \quad (\text{S31})$$

$$D_p \frac{\partial^2 p(x)}{\partial x^2} - \mu_p E(x) \frac{\partial p(x)}{\partial x} + G(x) - R(x) = 0 \quad (\text{S32})$$

The Schrödinger equations are based on the equilibrium of two contrasting forces which determine the charge carrier transport behavior in a semiconductor crystal: the drift force and the diffusion force\*. While the diffusion current of charge carriers is produced by charge carrier concentration differences within the p-type and the n-type semiconductor, the drift

---

\* Within the solar cell, both the drift and the diffusion current of charge carriers are always equal, determining therefore, different equilibrium conditions. In the dark the drift and the diffusion currents are in a specific intern equilibrium, producing thus only the built-in electrical field, if no external voltage is applied to the cell's terminals. Due to the production of additional charges under light exposure, the number of positive charges in the p-type layer and the number of negative charges in the n-type layer are further increased, and a new equilibrium of the drift-diffusion current is produced. If under this condition, a load is connected to the cell's terminals, an external drift current of electrons and holes defines, together with the internal drift current, another specific equilibrium.

current is produced by the net electric field\* appearing across the pin-type junction of the solar cell. In equations (S29) to (S32), the diffusion coefficients of electrons and holes  $D_n$  and  $D_p$  [cm<sup>2</sup>/s] are material-specific constants, which determine the random drift or spread of charge carriers in arbitrary directions within the semiconductor layers. This random diffusion is mainly limited to the depletion region, whose thickness is increased in the present heterojunction solar cell by use of the added intrinsic i-layer, made of the hybrid perovskite material. The diffusion coefficients for electrons and holes are calculated as follows<sup>56</sup>.

$$D_n = L_n^2 / \tau_n \quad (S33)$$

$$D_p = L_p^2 / \tau_p \quad (S34)$$

Where  $L_n$  [ m ] and  $L_p$  [ m ] are the diffusion lengths and  $\tau_n$  [ s ] and  $\tau_p$  [ s ] are the lifetimes of electrons and holes within the charge generation layer. The diffusion length of electrons and holes defines the pathway a charge carrier can diffuse until it is subjected to a recombination at the end of this pathway, and the lifetimes define the time interval in which the generated charge carrier can diffuse until its recombination does occur. Because of the extraordinarily long diffusion length, inherent to the perovskite layer material, the recombination effects in the intrinsic absorber layer resulting from a limited diffusion length can be neglected<sup>32</sup>, leading, therefore, to the simplification of  $R(x) = 0$  in equations (S29) to (S32), considering a pinhole free absorber layer. The mobility of electrons and holes  $\mu_n$  and  $\mu_p$  [m<sup>2</sup>/Vs] in equations (S29) to (S32), also called as motility<sup>32</sup>, determines how quickly a charge carrier can be moved through the solar cell as a function of the drift force. This drift

---

\* The net electric field represents, by reason of the superposition of the internal and the external electric fields, a barrier for the diffusion current. Whereas the internal field depends on the equilibrium of charge carrier concentrations of the solar cell, the external field is defined by the value of the cell's terminal voltage. If the cell is exposed to light, the external field is enhanced by the production of electrons within the n-type and holes within the p-type semiconductor.

force is a function of the device's internal electric field  $E(x)$  [V/m] as calculated by equation (S26)\*. The coefficients  $n(x)$  [ $\text{cm}^{-3}$ ] and  $p(x)$  [ $\text{cm}^{-3}$ ], in equations (S31) to (S34), are the charge carrier densities of electrons and holes, which are a function of the penetration depth  $x$ . In order to develop an analytical model which defines the shapes of the solar cell's dark I-V curve, another set of Schrödinger drift-diffusion equations is necessary, as given by equations (S35) and (S36).

$$D_n \frac{\partial^2 n(x)}{\partial x^2} + \mu_n E(x) \frac{\partial n(x)}{\partial x} - R(x) = 0 \quad (\text{S35})$$

$$D_p \frac{\partial^2 p(x)}{\partial x^2} - \mu_p E(x) \frac{\partial p(x)}{\partial x} - R(x) = 0 \quad (\text{S36})$$

By means of the solution of the four Schrödinger equations that define the electron and hole drift and diffusion in (equations S31, S32) and under privation of light (S35, S36), the four charge carrier currents as specified in equation (S4) can be calculated. **Photocurrent of electrons:** In a similar form as the electric field equation was derived from the second-order Poisson equation in equations (S21) to (S26), the analytical model for the generated current density of electrons  $J_{n\text{-photo}}$  (equation S4) is obtained by the following steps: (i) integration of the second-order electron drift-diffusion equation (S31) generating its general solution, which present two unknown integration constants; (ii) substitution of the boundary conditions (equations S37 and S39); in order to (iii) find an expression for  $J_{n\text{-photo}}$  as a solution of the obtained equation system. **Electron current in the dark:** The electron current density in the dark, here considered as recombination current density ( $J_{n\text{-dark}}$ ) is

---

\* The net electric field of a solar cell is defined by the superposition of its internal electric field and its external electric field. However, numerical simulations show that the net electric field in PSC is mainly defined by its internal electric field, and therefore, the use of the internal electric field for the replacement of the net electric field represents a good approximation. This concludes that the external electric field, which is a function of the photo-generated carriers, does not significantly perturb the net electric field as discussed in<sup>32</sup>, citing<sup>50</sup>.



obtained by a similar process, where, the derivation process starts, however, in step one with the formation of the general solution of the drift-diffusion equation which models the behavior of the cell in the dark (S35), using the same boundary conditions (equations S37 and S39). **Photocurrent of holes:** The analytical model of the generated hole current density ( $J_{p\text{-photo}}$ ) is obtained by a procedure using the steps of: (i) integration of the second-order hole drift-diffusion equation (S32), which results in its general solution, with two unknown integration constants; (ii) insertion of its boundary conditions (equations S38 and S40); obtaining (iii) the specific solution from the obtained equation system for the current density  $J_{n\text{-photo}}$ . **Hole current in the dark:** The current density of holes in the dark  $J_{p\text{-dark}}$  is obtained in a similar form as the hole current under exposition to light, using the drift-diffusion equation (S36) and using the same boundary conditions (equations S38 and S40).

The first Dirichlet-type boundary conditions in equations (S37) and (S38) specify the equilibrium hole and electron concentrations within the electron and the hole conductor layers at  $x = t_0$  and  $x = 0$ , which are the locations of the injections of the generated electrons and holes (Figure 1a).

$$n(x = t_0) = n(t_0) = N_{\text{Deff}} \quad (\text{S37})$$

$$p(x = 0) = p(0) = N_{\text{Aeff}} \quad (\text{S38})$$

At equilibrium, these electron and hole concentrations are equal to the effective doping concentrations of the acceptor molecules ( $N_{\text{Aeff}}$ ) and donor molecules ( $N_{\text{Deff}}$ ). The second Dirichlet-type boundary conditions consider the undesired evasion of electrons and holes at the sites of the recombination current densities of electrons and holes at penetration depth  $x = 0$  and  $x = t_0$  (Figure 1a). These radiation-independent Dirichlet-type boundary conditions are specified by the front and back recombination currents  $J_f$  and  $J_b$  in equations (S39) and

(S40)\*.

$$J_n(x=0) = J_f = q s_n \Delta n = q s_n \left( n_i - \frac{n_i^2}{N_{Aeff}} \right) \quad (S39)$$

$$J_p(x=t_0) = J_b = q s_p \Delta p = q s_p \left( p_i - \frac{p_i^2}{N_{Deff}} \right) \quad (S40)$$

Where  $s_n = s_f$  is the front charge conduction layer's surface recombination velocity of electrons, while  $s_p = s_b$  is the back charge conduction layer's surface recombination velocity of holes. These four boundary equations together with the solution of the Poisson equation are used in order to derive the analytical solar cell model of perovskite solar cells, as presented in SI-1.1 to SI-1.3. In this context, it has to be mentioned that the substitution of the equation of the electric field (S26) in the drift-diffusion equations enables the modeling of the electron and hole current as a function of the terminal voltage  $V$  for both cases, under exposition of the solar cell to reference light and in the dark.

Furthermore, the substitution of some other model variables, by expressions related to known physical effects, results in a reduction of the total quantity of model variables in the multidimensional optimization. Therefore, the charge carrier mobilities  $\mu_n$  and  $\mu_p$  in equations (S29) to (S34) do not represent a multidimensional model variable in Tables 2 and 3. This occurs as the Einstein expressions are considered for the substitution in the drift-

---

\* The boundary equations of the Poisson equation (S23 and S24) are both defined for the same variable, which is the electrostatic potential  $\phi$ , which facilitates therefore, the solution of this second-order differential equation. However, in the case of the drift-diffusion differential equation, the first boundary equation specifies the electron density (S37), while the second boundary equation specifies the current density of electrons (S39). Thus, the solution of the general equation is obtained differently. In a first step, the first boundary equation (S37) is substituted in the general solution of the drift-diffusion equation, which results in a solution of  $n(x)$  with a remaining unknown integration constant. Then, in a second step the term of  $n(x)$  is substituted in the current density equation (S29), obtaining therefore, an electron current density equation  $J_n(x)$  with an unknown integration variable. Now the second boundary equation (S39) can be substituted in equation of  $J_n(x)$  in order to find an expression for the remaining integration constant, which is substituted in  $J_n(x)$  order to obtain a solution for photogeneration current  $J_{n-photo}(x=t_0)$ . This process is then repeated with the drift diffusion equations and its boundary conditions for holes, finding the hole generation current  $J_{p-photo}(x=0)$  (Figure 1a). For the recombination current, the derivation process is repeated under consideration of  $G(x) = 0$ , using the drift-diffusion equation in (S35) and (S36), instead of (S31) and (S32). The obtained four current densities can be used for its substitution in the complete model in equation (S4).

diffusion equations. The Einstein expressions for electrons and holes are given by equations (S41) and (S42).

$$\frac{\mu_n}{D_n} = \frac{q}{k_B T} = \frac{1}{V_t} \quad (\text{S41})$$

$$\frac{\mu_p}{D_p} = \frac{q}{k_B T} = \frac{1}{V_t} \quad (\text{S42})$$

Considering that for a given semiconductor temperature  $T$  [K] a fixed thermal voltage  $V_t$  is obtained, the mobility  $\mu_n$  can be substituted by the following equation

$$\mu_n = D_n / V_t \quad (\text{S43})$$

In an analog form the mobility of holes can be substituted as follows

$$\mu_p = D_p / V_t \quad (\text{S44})$$

Such substitutions can be considered as the drift and the diffusion forces are permanently in equilibrium. Therefore, the drift coefficients are in a specific fixed relation to the diffusion coefficients, which means that knowing one of them, e.g. the diffusion coefficients of electrons and holes, the others (the drift coefficients) can be modeled by expressions (S43) and (S44). These expressions are used for the substitution of the charge carrier mobilities  $\mu_n$  and  $\mu_p$  in the four drift-diffusion equations (S31, S32, S35, and S36).

In order to simplify mathematically the derivation process of drift diffusion equations (S31, S32, S35, and S36), it is of advantage to transform these four equations in a normalized form. For the differential equations from which the photocurrent is derived (S31, S32), this normalization considers the following steps: (i) the charge carrier generation rates  $G(x)$  in equation (S31) and (S32) are substituted by the expression in (S18), (ii) the generation rate

of charge carriers at the top surface of the absorber layer ( $G_{eff}$ ) in (S18) is substituted by equations (S45) and (S46), (iii) the division  $D_n$  and  $D_p$  in the obtained equations lead to the normalized model of the drift-diffusion equations (S47 and S48), which are specified as function of the so defined normalized generation rates of electron and holes  $G_n$  and  $G_p$ , both measured in units of  $[m^{-5}]$ .

$$G_{eff} = G_n D_n \quad (S45)$$

$$G_{eff} = G_p D_p \quad (S46)$$

It can be seen in equations (S47) and (S48) that also an expression of a normalized electric field  $\varepsilon_n [1/m]$  is adopted, which is specified by equation (S50).

$$\frac{\partial^2 n(x)}{\partial x^2} + \varepsilon_n \frac{\partial n(x)}{\partial x} + G_n e^{-x/\lambda_{ave}} = 0 \quad (S47)$$

$$\frac{\partial^2 p(x)}{\partial x^2} - \varepsilon_n \frac{\partial p(x)}{\partial x} + G_p e^{-x/\lambda_{ave}} = 0 \quad (S48)$$

This substitution of  $\varepsilon_n$  in equations (S47) and (S48) considers some further steps of the mathematical treatment of the general drift diffusion equations for its normalization: (iv) the terms  $\mu_n$  and  $\mu_p$ , which are present in the second term of the drift diffusion equations (S31) and (S32), are substituted by the expressions (S43) and (S44), (v) the appearing diffusion coefficient in the numerator of the second term is cut out by reason of the general division of  $D_n$  (step iii), and (vi) the remaining expression in the second term of the drift diffusion equations ( $E / V_t$ ) is substituted by expression (S49), which is here considered as the normalized electric field  $\varepsilon_n [1/m]$ . Thus  $\varepsilon_n$  in equations (S47) and (S48) is defined as a normalized electric field, which is calculated as follows.

$$\varepsilon_n = E / V_t \quad (\text{S49})$$

A similar normalization, and thus simplification, is considered for the drift-diffusion equations for the dark condition (S35) and (S36), which result therefore, to the normalized drift diffusion equations in the dark as presented in (S50) and (S51).

$$\frac{\partial^2 n(x)}{\partial x^2} + \varepsilon_n \frac{\partial n(x)}{\partial x} = 0 \quad (\text{S50})$$

$$\frac{\partial^2 p(x)}{\partial x^2} - \varepsilon_n \frac{\partial p(x)}{\partial x} = 0 \quad (\text{S51})$$

After the finalization of the derivation process, the equations for the electron and hole currents under the cell's light exposure and in the dark are obtained as function of the normalized variables  $G_n$ ,  $G_p$  and  $\varepsilon_n$ . The non-normalized true model variables  $E$ ,  $V_t$ ,  $D_n$ ,  $D_p$ ,  $G_{\text{eff}}$ ,  $\mu_n$ ,  $\mu_p$  are obtained by back substitution using equations (S50), (S49), (S48), (S47), (S46), (S44) and (S43), which results in the complete analytical model as presented in (Chapters 1.1 to 1.3). Finally, it has to be remarked that although analytical PSC model, presented in Sun et al., (2015), considers some simplifications as mentioned within the discussions related to its presentation (Supplementary Sections 1.1 to 1.3) and its derivation (Supplementary Section 1.4) it results in low dissimilarities if the simulated I-V curves are compared with the measured curves of a manufactured perovskite pin-type solar cell<sup>32</sup>.

### **Detailed optimization setup configuration**

The solar cell properties and absorber layer thickness as obtained in (Sun et al., 2015)<sup>32</sup> by model fitting and one-dimensional optimization of the absorber layer thickness, using the measured UI-curves of a pin-type perovskite solar cell, are used as initial configuration for

the present multidimensional optimization. In order that the model as specified in<sup>32</sup> fits to the measured VI-curves  $J_{\text{dark}}(V)$  and  $J_{\text{light}}(G, V)$  (equation S3), the authors defined first by use of the Optical Transfer Matrix (OTM) method, the fundamental optical parameters of the here analysed cell, which are: (i) the effective generation of charge carriers  $G_{\text{eff}} = 1.4356 \times 10^{13} \text{ cm}^{-3}\text{s}^{-1}$  and (ii) the average optical decay length  $\lambda_{\text{ave}} = 100 \text{ nm}$ , which are both thickness independent material specific constants of the used perovskite absorber layer. By means of equation (S20), the authors calculate the maximal or total generation of free charges  $G_{\text{max}} = 1.4356 \times 10^{17} \text{ cm}^{-2}\text{s}^{-1}$  based on a measured short circuit current of  $qG_{\text{max}} = 23 \text{ mA/cm}^2$ . The obtained the electron and hole diffusion coefficients and the built-in voltage values for the used cell were obtained in<sup>32</sup> from further references and are specified as  $V_{\text{bi}} = 0.78 \text{ V}$ ,  $D_n = D_p = 0.05 \text{ cm}^2/\text{s}$  (Table 2). For a non-optimized manufactured solar cell the detailed model parameters, which specify the properties of the pin-type cell, were obtained in<sup>32</sup> by model fitting using the algorithm 'lscurvefitt' of the Mablalab<sup>TM</sup> program. This algorithm minimizes the sum of the least square deviations between the values of the measured and the modeled VI-curves. Using the obtained material properties by model fitting the authors obtained by means of an one dimensional model optimization an ideal absorber layer thickness of  $t_0 = 450 \text{ nm}$ . For an manufactured cell of  $t_0 = 450 \text{ nm}$  the authors obtained the following model properties by use of a further model fitting:  $s_f = 200 \text{ cm/s}$  and  $s_b = 19.2 \text{ cm/s}$ ,  $\Delta n = 8.426 \times 10^6 \text{ cm}^{-3}$ ,  $\Delta p = 1.3003 \times 10^8 \text{ cm}^{-3}$  (Table 2), leading to an cell efficiency of  $\eta = 15.7\%$ , a short circuit current density of  $22.7 \text{ mA/cm}^2$  and an open circuit voltage of  $V_{\text{OC}} = 0.85 \text{ V}$  (Figure 3), while the recombination current of electron and holes were calculated with  $J_{f0} = 2.7 \times 10^{-13} \text{ mA/cm}^2$  and  $J_{b0} = 4.0 \times 10^{-13} \text{ mA/cm}^2$ . The measured semiconductor temperature was  $T_a = 27.41 \text{ }^\circ\text{C}$ , resulting in the absolute cell temperature of  $T = T_a + 273.15 \text{ K} = 300.56 \text{ K}$ , and a thermal voltage of  $V_t = 25.9 \text{ mV}$ , at the moment when the VI-curves were measured.

## SI-2. Most sensible model variables

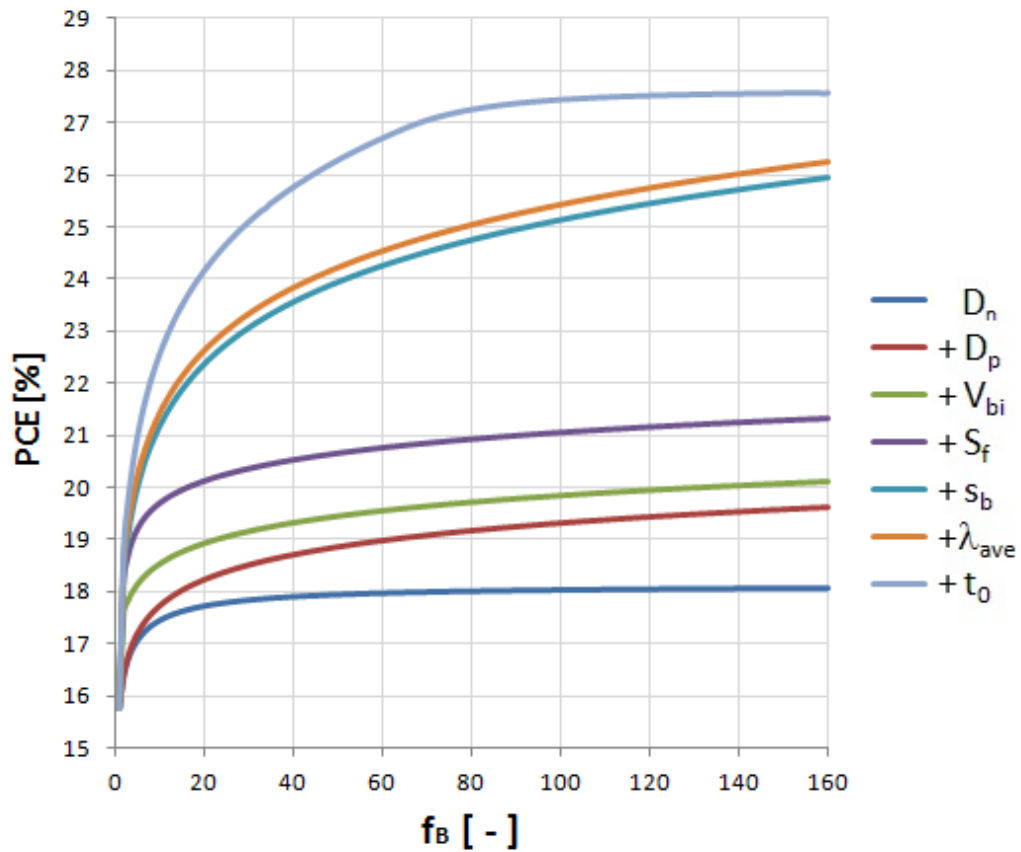
Solar cell designers should know which cell properties or manufacturing parameters are most important in order to modify these variables by priority for obtaining the most significant increase of solar cell device efficiency. Table 1 summarizes these properties and parameters. Considering e.g. a boundary modification factor of  $f_B = 100$ , the one-dimensional optimization of the effective surface recombination velocity  $s_f$  and the diffusion coefficient  $D_n$  led to the two highest efficiency growths, increasing from an initial value of 15.7 % to 18.4 % and 18.1 %. For two-dimensional optimizations the front and back recombination velocities,  $s_f$  and  $s_b$  led to the best efficiency of 22.5 %, whereas the second best efficiency of 19.9 % was obtained by either of the following combinations: (i) the diffusion lengths  $D_p$  and  $D_n$ ; (ii)  $D_n$  with  $s_b$ ; and (iii)  $t_0$  with  $\lambda_{ave}$  (Table 1). Thus, in general, it can be recommended that the model parameters of the perovskite cell should be improved with the following sequence of priority: (i) the front effective surface recombination velocity; (ii) both the front and the back surface recombination velocities; (iii) the diffusion coefficients of electrons and holes; (iv) the average optical decay length; (v) the absorber layer thickness; and (vi) the built-in voltage. In this context of subsequent inclusion of variables, the cells thickness  $t_0$  should always be adjusted as a function of  $\lambda_{ave}$ , and the remaining material properties of the solar cell, as can be concluded from the comparison of the blue vertex lines in Figures 2e and 2f.

### **SI-3. Subsequent inclusion of variables and variation of the boundary conditions in multidimensional optimization processes**

The contribution of each of the variables in a multidimensional optimization is accounted for by the validation of the efficiency increases under successive inclusion of model variables in the optimization process. Optimizations under these considerations are accomplished as a function of individual boundary conditions, which are specified by a variable boundary expansion factor  $f_B$  in Fig. S1. The optimizations in Figure S1 start with the one-dimensional optimization of the diffusion coefficient of electrons ( $D_n$ ), considering a series of 160 optimizations, where  $f_B$  varies from 1 to 160 ( $f_B \in \mathbb{N}$ ). By successive inclusion of further model variables in the optimization process, it is then shown how the efficiency increases, accomplishing for each variable included a new set of 160 optimizations. The variables in Figure S1 are included in the optimization process in the following arbitrary sequence: (i)  $D_n$ , (ii)  $D_p$ , (iii)  $V_{bi}$ , (iv)  $S_f$ , (v)  $S_b$ , (vi)  $\lambda_{ave}$  (vii)  $t_0$ . The stepwise inclusion shows that each new variable added results in an individual and variable inherent increase of the maximal attainable PCE (Fig. S1) considering different boundary expansion factors  $f_B$  as specified in equation (5). It is shown that the most significant increase of the PCE is obtained for small variable improvements with boundary expansion factors of  $f_B < 30$ . In these cases, the PCE increases from an initial 15.7 % to a maximum of 25.2 %. For  $f_B = 160$  the inclusions of  $S_b$  (+ $S_b$ ) result in the most significant efficiency increase, where PCE grows by 4.6 %, while the second highest increase of 2.5 % is observed for (+ $t_0$ ). The inclusion of the  $\lambda_{ave}$  (+ $\lambda_{ave}$ ) leads to the smallest efficiency increase. This is expected, as the reduction of  $\lambda_{ave}$  by its own leads to negligible efficiency growth, and only its tuned reduction with a decreasing absorber layer thickness leads to a significant rise of the efficiency as can be seen by the blue vertex lines in Figs. 2e and 2f.



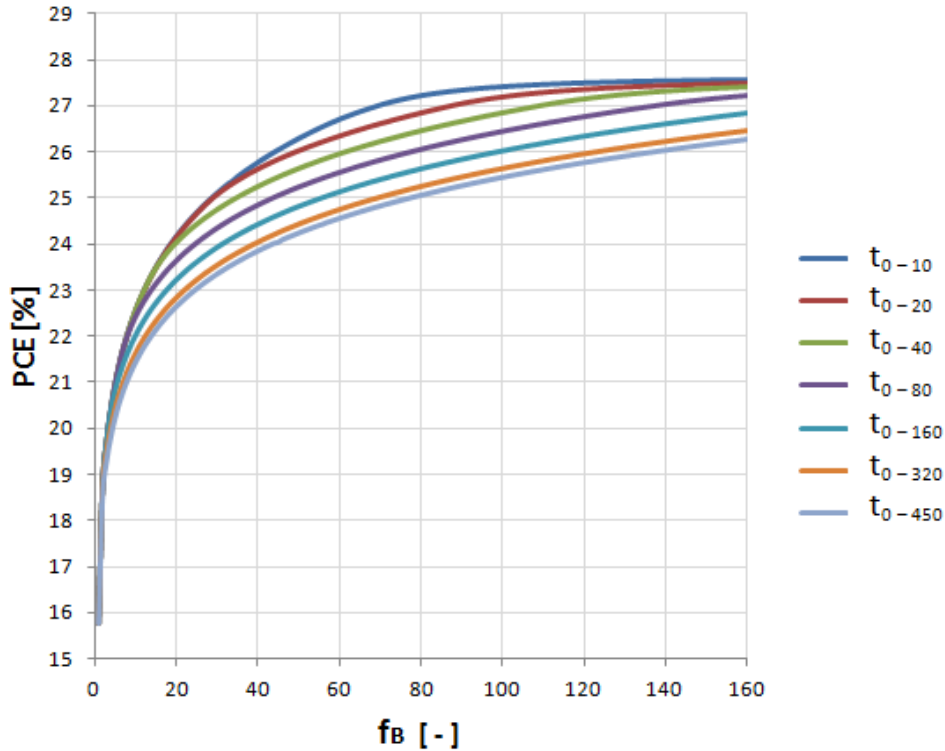
The Supplementary Figure S2 shows how the curve of the highest efficiency in Fig. S1 is reduced because of several specifications for the minimal necessary thickness for the absorber layer. A set of seven different minimum absorber layer thicknesses ranging from  $t_{0-\min} = 10$  to 450 nm is imposed to the optimization process. We consider that the thinner absorber layer with  $t_0 = 10 \dots 320$  nm presents the same generation rate of charge carriers as the absorber layer of 450 nm thickness, due to adequate light trapping effects, which tunes the average optical decay length, without introducing additional recombination effects



**Supplementary Figure S1** | Optimized efficiency as function of the boundary expansion factor  $f_B$  considering optimizations, which include the following sets of variables: (i) only the diffusion coefficient of electrons ( $D_n$ ); (ii) the combination of  $D_n$  and  $D_p$  ( $+D_p$ ); (iii) the variables  $D_n$ ,  $D_p$  and  $V_{bi}$  ( $+V_{bi}$ ); (iv) the variables  $D_n$ ,  $D_p$ ,  $V_{bi}$  and  $S_f$  ( $+S_f$ ); (v) the variables  $D_n$ ,  $D_p$ ,  $V_{bi}$ ,  $S_f$  and  $S_b$  ( $+S_b$ ); (vi) the variables  $D_n$ ,  $D_p$ ,  $V_{bi}$ ,  $S_f$ ,  $S_b$  and  $\lambda_{ave}$  ( $+\lambda_{ave}$ ); (vii) the variables  $D_n$ ,  $D_p$ ,  $V_{bi}$ ,  $S_f$ ,  $S_b$ ,  $\lambda_{ave}$  and  $t_0$  ( $+t_0$ ).

It can be seen that for the least ideal manufacturing method, which considers an absorber layer thickness of  $t_{0\min} = 450$  nm, the maximal attainable efficiency is reduced only by

approximately 1.4 % with  $f_B = 160$ . At  $f_B = 60$  such an efficiency loss is more significant showing 2.3 % and it occurs probably by the higher number of recombination centers at the transition surface in-between the perovskite crystals in the absorber layer. For very high and low  $f_B$  values, there are insignificant PCE losses for the 20 nm absorber coatings when compared with the most efficient 10 nm coatings.



**Supplementary Figure S2** | Optimized efficiency as a function of the boundary expansion factor  $f_B$  considering the reduction of the maximal possible efficiency in an optimization by use of the complete set of six model variables ( $D_n$ ,  $D_p$ ,  $V_{bi}$ ,  $S_f$ ,  $S_b$ ,  $\lambda_{ave}$ ). Specific manufacturing conditions impose a minimal necessary absorber layer thicknesses ( $t_0 = t_{0-min}$ ) in order to avoid pinholes. For  $t_{0-min}$  the following minimal thicknesses are considered: (i) 10 nm, (ii) 20 nm, (iii) 40 nm, (iv) 80 nm, (v) 160 nm, (vi) 320 nm and (vii) 450 nm.

#### SI-4. Manufacturing recommendations for efficiency enhancement

Efficiency increases can be accomplished not only by optimizations of one or two material properties of the PSC, but most effectively as a function of multiple cell properties and the absorber layer thickness, which constitute a multidimensional space of variables to which the solar cell efficiency is sensitive. The following specific recommendations are proposed here in order to increase the efficiency of pin-type perovskite cells in such a variable space.

#### **SI-4.1. Front and back surface Recombination Velocities**

In order to increase the efficiency of PSC, the effective Surface Recombination Velocity of the front ( $s_f$ ) and the back surfaces ( $s_b$ ) should be reduced further e.g. by doping, which results in lower trap densities<sup>54,55</sup>, and principally by passivation techniques<sup>54</sup>. Such passivating techniques include the use of: (i) fullerene interlayers between the absorber and the charge conduction layers; (ii) supramolecular halogen complexation, or the utilization of (iii) type thiophene or (iv) type pyridine Lewis bases. Passivation techniques are of special importance for grain sizes of perovskite crystals which are smaller than 5  $\mu\text{m}$ , thus mitigating the high density of recombination sites related to small grain sizes<sup>54</sup>. Isolated perovskite crystals present a two to three orders of magnitude lower effective surface recombination velocity than crystals used in commercially available solar cells<sup>9</sup>. Therefore, the crystal size of the absorber layer should be increased as much as possible in order to reduce the transition surface area between the crystals in the absorber layer, and accordingly, reduce the active trap states and the surface recombination velocities.

#### **SI-4.2. Diffusion Coefficients of electrons and holes**

In order to increase the diffusion coefficients of the electrons and holes, the perovskite material should be modified in an appropriate form. As shown in Fig. 2c, especially large efficiency improvements can be obtained by an increase of  $D_p$  if  $D_n$  is at least increased to 0.3  $\text{m}^2/\text{s}$ . As the diffusion coefficients of electrons and holes are determined by the expressions (S33) and (S34), they can be increased by either, (i) the augmentation of the electron or hole diffusion lengths  $L_n$  and  $L_p$ , or alternatively (ii) by the reduction of its lifetimes  $\tau_n$  and  $\tau_p$ . High diffusion lengths of electrons and holes, of approximately 1.9  $\mu\text{m}$  and 1.5  $\mu\text{m}$ , were observed for  $\text{CH}_3\text{NH}_3\text{PbI}_{3-x}\text{Cl}_x$  perovskite solar cells, as obtained by indirect measurements with electron beam-induced currents (EBIC)<sup>12</sup>. A reduction of

recombination sites by a Lewis Base passivation resulted not only in a reduced number of trap states at the perovskite crystal terminations but also enabled an excellent diffusion length of charge carriers with values higher than 3  $\mu\text{m}$ <sup>68</sup>. The reduction of the electron or hole lifetimes is related to the fast decay of their photoluminescence<sup>13</sup> and can be obtained e.g. if the coated PSC is treated by a post-annealing process with a temperature of 160 °C<sup>13</sup>. Such a process increases the PCE and reduces the lifetime of PSC charge carriers from 44 ns to 22.6 ns as shown by Song et al.<sup>13</sup>. As the charge separation time in a PSC operates at a much smaller time scale of only 100 fs<sup>7</sup>, such a shorter lifetime should not hinder this charge separation as the diffusing electrons and holes are separated very fast. Another method in order to reduce the charge carrier lifetime is obtained by the incorporation of 560 nm long rutile TiO<sub>2</sub> nanorods into a CH<sub>3</sub>NH<sub>3</sub>PbI<sub>3</sub> perovskite cell<sup>57</sup>. Nanorods are a network structure of single-crystal-like short nanowires, which can be manufactured by e.g. the surfactant assisted oriented attachment mechanism<sup>58,59</sup>. Nanorods do additionally improve the extraction of charge carriers by decreasing the time interval which is necessary to transport the separated charge carriers within the charge conduction layers<sup>57</sup>. Therefore, they should also reduce the recombination losses related to these layers, as the time during which electrons and holes are present within the CTL is shorter.

#### **SI-4.3. Average optical decay length**

As each of the existing perovskite materials has an individual inherent average optical decay length ( $\lambda_{\text{ave}}$ ), a perovskite material which presents a short  $\lambda_{\text{ave}}$  should be selected, e.g. the MAPbI<sub>3</sub> molecule used here. Actually, if the values of absorption coefficients of MAPbI<sub>3</sub> and GaAs cells are compared, as a function of the wavelength, it can be observed that the former has significantly higher absorption coefficients than the latter for basically the whole wavelength range<sup>14</sup>. This is remarkable as GaAs cells are among the highest efficiency single

junction state-of-the-art solar cells, presenting a high PCE of 28%<sup>20</sup>, which is, by the way, the value of theoretical efficiency limit of this cell type<sup>14</sup>. Actually, the hypothetical efficiency limit of an ideal MAPbI<sub>3</sub> cell, which does not consider recombination losses, is 30 % by reason of its light absorption<sup>14</sup>. Furthermore, it can be seen from absorbance figures published elsewhere<sup>15,60</sup> that the absorbance values of a formamidinium lead trihalide cell (FAPbI<sub>3</sub>), are still significantly higher than the corresponding values of the most efficient MAPbI<sub>3</sub> cell. This behavior is observed over almost the whole analyzed spectrum range up to 800 nm, which should, therefore, lead to an upper theoretical limit > 30 % for the FAPbI<sub>3</sub> cell. Additionally, the correct selection of the post-annealing temperature and time will increase the absorbance values of perovskite solar cells<sup>61,62</sup>. Finally, different light trapping techniques<sup>63</sup> lead to a considerable increase of light absorption in PSC. If e.g. distributed size metal Nano Particles (NPs) are inserted into the absorber layer of the perovskite solar cell, a collective oscillation of the conduction band electrons occurs, by reason of the optical excitation of the NPs with light waves, which own a frequency similar to the NP's inherent resonance frequency. This oscillation provokes a strong spherical scattering of light partitioning from each of the NPs, which leads then to the plasmonic light trapping effect<sup>17,18</sup>. Such a light trapping effect can be explained as the spherical scattering increases the total optical path length of the solar irradiance rays within the solar cell, which, therefore, increases its absorption<sup>18</sup> and decreases its average optical decay length. As this resonance frequency is a function of the NP's size, a carefully engineered and tuned distribution of the particle sizes, added to the solar cell's absorber, should result in an increase in the ultraviolet and visible-light absorption\*. The light trapping effect inherent to plasmonic NPs can be modeled by the Mie theory and numerical simulations predict the highest increase of the short-circuit current for PSCs which present the thinnest absorption layer<sup>18</sup>. The authors

---

\* Such sizable spherical NP can be cost effectively synthesized and deposited by Nanosphere Lithography (NSL)<sup>64,65</sup>.

show that  $I_{sc}$  can increase significantly by 4.3 times for PSC with 10 nm thick absorber layer if lumpy silver (Ag) particles are distributed on the back side of a 10 nm thin absorber layer of a PSC. As thinner absorber layers without plasmonic NPs present a reduction of  $I_{sc}$ <sup>32</sup>, a current augmentation by reason of light trapping effects has to outweigh this reduction, thus resulting in a net increase of  $I_{sc}$  as well as the PCE. First results with manufactured PSC show an increase of  $I_{sc}$  by 1.2 times on average, whereas the efficiency increases by 22 % or by the factor 1.22 times<sup>66</sup>. The author used a 130 nm thick PSC absorption layer and added distributed size nanoparticles with average diameter of 11 nm. However, the highest simulated  $I_{sc}$  increased 1.5 times<sup>18</sup>, rather than 1.2 times<sup>66</sup> for this absorber layer thickness. This difference may be ascribed to undesired conduction effects related to the nanoparticles or to pinholes related to the thinner absorber layer. It can be noted from this discussion that plasmonic nanoparticles do increase the PCE and are most effective if inserted into very thin layers of 10 to 30 nm, which can be manufactured e.g. by use of the Solvent-Solvent Extraction technique without the appearance of pinholes<sup>44</sup>. Such cells would lead to a significant increase of the  $I_{sc}$  when compared to cells with the same thickness and without plasmonic nanoparticles<sup>18</sup>, which results in a relevant increase of the PCE if further material properties are concomitantly improved. This is in agreement with the results obtained in this paper, as shown in Table 2, Figure 2f, Figures 3, and Supplementary Figures S1 and S2.

#### **SI-4.4. Absorber layer thickness**

The absorber layer thickness  $t_0$  of a PSC should be adjusted as a function of the attained reduction of the average optical decay length  $\lambda_{ave}$  (Figs 2e, 2f). This can be best accomplished by use of a large surface deposition technique denominated as Solvent-Solvent Extraction technique (SSE)<sup>44</sup>. The SSE allows the coating of ultra-thin and

homogeneous perovskite layers with thicknesses as small as 20 nm<sup>\*</sup>. Here it should be mentioned that the specific condition of thin absorber layers is relaxed, to some extent, in the multidimensional optimization, allowing for thicker absorber layers, which can be seen by the comparison of the blue vertex lines in Figs. 2e and 2f. As in this work, only optimized solar cells are considered, the short circuit currents of cells with different absorber layer thicknesses are very similar to the ones shown in Figure 3. This effect appears as a correct thickness tuning as a function of the obtained average optical decay length led to a comparable absorption of photons for different layer thicknesses.

#### SI-4.5. Built-in voltage

The built-in voltage of the PSC should be increased, which can be accomplished if the absorber layer is manufactured by a two-step solution deposition method at elevated temperatures as shown in Zhu et al.<sup>19</sup>. E.g. in order to constitute a CH<sub>3</sub>NH<sub>3</sub>PbI<sub>3</sub> absorber layer, a substrate coated with a TiO<sub>2</sub>-PbI<sub>2</sub> film has to be immersed in a CH<sub>3</sub>NH<sub>3</sub>I solution heated to 70 °C, resulting in a built-in voltage of  $V_{bi} = 0.89 \text{ V}$ <sup>†</sup>. Zhu et al.<sup>19</sup> analyze several solution temperatures within the range of 25 to 70 °C and show that high solution temperatures also result in the following additional advantages: (i) the crystal grain size increases; (ii) the charge transport and extraction ability increases; and (iii) the recombination rate decreases. An extraordinary high built-in voltage of  $V_{bi} = 1.19 \text{ V}$  was obtained for a CH<sub>3</sub>NH<sub>3</sub>PbI<sub>3-x</sub>Cl<sub>x</sub> based PSC<sup>67</sup>, where the built-in voltage was measured in the dark by determination of the electric field using the capacitance-voltage measurement technique. The authors confirmed the measurement of this high built-in voltage by use of

---

\* The SSE method is a very simple method, which can be processed at room temperature and results in high-quality perovskite absorber layers. It presents a high uniformity of its grown crystals and allows for a very exact thickness control over the deposition of the absorber layer. E.g. in order to constitute a MAPbI<sub>3</sub> perovskite cell the process can be started with a stoichiometric MAPb<sub>2</sub> precursor solution, which is diluted in a N-methyl-2-pyrrolidone solvent in order to be applied by a coating technique, e.g. spin-coating, after which the coated substrate is immediately bathed in Diethyl Ether and then dried in ambient air.

† As shown in (Fig. 2b) a  $V_{bi}$  of 0.89 V is sufficient as it increases the PCE by 1 % in a one-dimensional PCE optimization, obtaining an optimized efficiency, which is only circa 0.2 % lower than the maximal attainable PCE in this single dimension function space.

the Kelvin Probe Force Microscopy (KPFM) measurement technique. In order to increase the built-in voltage additionally an appropriate band gap engineering of the semiconductor materials should be deployed, which results therefore, in an improved electron and hole extraction and increases the built-in voltage  $V_{bi}$  by an improved tuning of the effective doping concentrations (equation S11), which also increases the built-in potential difference  $\Delta\phi_{bi}^*$ .

#### **SI-4.6. Quantity of excess holes and electrons**

The number of excess holes and electrons that participate in the recombination process  $\Delta p = p - p_0$ , and  $\Delta n = n - n_0$ , as used for the modeling in equations (S6) and (S7), are already located within the region of the highest efficiency (Fig. 2d). Furthermore, it can be seen that  $\Delta p$  and  $\Delta n$  are not improved by the optimization algorithm (Tables 2 and 3). Therefore, we believe that improvements for this variable are not relevant for the optimization of the present solar cell and were, by this reason, not considered here.

---

\* In the present solar cell with non-optimized band gap the built-in potential difference is  $\Delta\phi_{bi} = 0.3$  eV (Fig. 1a), leading to a built-in voltage of  $V_{bi} = 0.78$  V as calculated by (equation 11).



#### SI-4.7. Nomenclatures:

A	Photocurrent substitution parameter [ - ],
B	Photocurrent substitution parameter [ - ],
$D_n$	Diffusion coefficient of electrons [ $\text{m}^2/\text{s}$ ],
$D_p$	Diffusion coefficient of holes [ $\text{m}^2/\text{s}$ ],
E	Built-in electrical field [ $\text{V}/\text{m}$ ],
$E_g$	Effective band gap energy [ $\text{eV}$ ],
$f_B$	Boundary expansion factor [ - ],
$G_{AM1.5}$	Solar irradiance with air mass 1.5 [ $\text{W}/\text{m}^2$ ]
$G(x)$	Generation rate of charges as function of x [ $\text{s}^{-1}\text{m}^{-3}$ ],
$G_{\text{eff}}$	Effective charge carrier generation [ $\text{s}^{-1}\text{m}^{-3}$ ],
$G_n$	Charge generation of electrons [ $\text{m}^{-5}$ ],
$G_p$	Charge generation of holes [ $\text{m}^{-5}$ ],
$G_{\text{max}}$	Maximal or total charge carrier generation [ $\text{s}^{-1}\text{m}^{-2}$ ]
$J_{b0}$	Electron recombination current density of the back charge conduction layer at $x = t_0$ [ $\text{A}/\text{m}^2$ ],
$J_b(x)$	Electron recombination current density of the back charge conduction layer as function of x [ $\text{A}/\text{m}^2$ ],
$J_{\text{dark}}$	Measurable current density in the dark [ $\text{A}/\text{m}^2$ ],
$J_{f0}$	Hole recombination current density of the front charge conduction layer at $x = 0$ , [ $\text{A}/\text{m}^2$ ],
$J_f(x)$	Hole recombination current density of the front charge conduction layer as function x [ $\text{A}/\text{m}^2$ ],
$J_{\text{light}}$	The measurable current density under light exposure [ $\text{A}/\text{m}^2$ ],
$J_{\text{MPP},i}$	Maximal Power Point Current density [ $\text{A}/\text{m}^2$ ],
$J_{\text{photo}}$	Internal photo-generated current density [ $\text{A}/\text{m}^2$ ],
$J_{\text{sc}}$	Short-Circuit Current [ $\text{A}/\text{m}^2$ ],
$k_B$	Boltzmann constant $1.38064852 \times 10^{-23}$ [ $\text{J}/\text{K}$ ],
M	Dimensionless ratio in the Beer-Lambert law [ - ],
$N_{\text{Aeff}}$	Effective doping concentration of the electron acceptor molecules [ $\text{m}^{-3}$ ],
$N_{\text{Deff}}$	Effective doping concentration of the electron donor molecules [ $\text{m}^{-3}$ ],

$n$	Electron density [ $\text{m}^{-3}$ ],
$n_0$	Electron density under thermal equilibrium [ $\text{m}^{-3}$ ],
$n_i$	Inherent carrier density of the undoped charge conduction layers [ $1/\text{m}^3$ ],
$p_0$	Hole density in thermal equilibrium [ $\text{m}^{-3}$ ]
$P_{\text{MPP}}$	Maximal Power Point Power [ $\text{W}/\text{m}^2$ ],
$q$	Electric charge of an electron or hole [ $\text{As}$ ],
$R(x)$	Recombination rate of charges as function of $x$ [ $\text{s}^{-1}\text{m}^{-3}$ ],
$S_f$	Surface recombination velocity of electrons ( $s_n$ ) related to the front hole conduction layer [ $\text{m}/\text{s}$ ],
$S_b$	Surface recombination velocity of holes ( $s_p$ ) related to the back electron conduction layer [ $\text{m}/\text{s}$ ],
$T$	Cell temperature [ $\text{K}$ ],
$t_0$	Absorber layer thickness [ $\text{m}$ ],
$t_{0-\text{min}}$	Minimal absorber layer thickness [ $\text{m}$ ],
$t_{0-\text{min}}$	Minimal necessary absorber layer thickness [ $\text{m}$ ],
$V$	Terminal Voltage of the solar cell [ $\text{V}$ ],
$V_{\text{bi}}$	Built-in voltage [ $\text{V}$ ],
$V_{\text{MPP}}$	Maximal Power Point Voltage [ $\text{V}$ ],
$V_{\text{oc}}$	Open-circuit Voltage [ $\text{V}$ ],
$x = 0 \dots t_0$	Solar irradiance penetration depth [ $\text{m}$ ],
$X_j = X_1 \dots X_9$	$X_j$ is one of the nine model variables of the PSC model,
$X_{j,\text{me}}$	A model variable extracted from the measured I-V curve, $X_j$ , is one of the nine model variables of the PSC model,
$X_{j-\text{min}} \dots X_{j,\text{max}}$	Variable expansion range for the variable $j$ ,
$\alpha_b$	Back recombination current scaling coefficient [ - ],
$\alpha_f$	Front recombination current scaling coefficient [ - ],
$\Delta n$	Excess number of electrons in the n-type layer [ $\text{m}^{-3}$ ],
$\Delta p$	Excess number of holes in the p-type layer [ $\text{m}^{-3}$ ],
$\varepsilon$	Permittivity [ $\text{Fm}^{-1} = \text{C V}^{-1}\text{m}^{-1} = \text{AsV}^{-1}\text{m}^{-1}$ ],
$\varepsilon_n$	Normalized electrical field [ $1/\text{m}$ ],
$\eta_i$	Optimized PCE for the $i$ -th optimization iteration [%],
$\eta_{\text{max}}$	Optimized efficiency value [%],

$\lambda$	Wavelength of the solar radiation irradiance [m],
$\lambda_{ave}$	Average optical decay length [m].
$\mu_n$	Drift coefficient or mobility of electrons [ $m^2V^{-1}s^{-1}$ ]
$\mu_p$	Drift coefficient or mobility of holes [ $m^2V^{-1}s^{-1}$ ]
$\rho$	Density of charge carriers [ $m^{-3}$ ],

**Indexes:**

$i = 1 \dots N$	Iterations in the optimization of the efficiency,
$k = 1 \dots M$	Iterations in the optimization of the power curve,
$j = 1 \dots 9$	Index which counts the nine variables,

## REFERENCES

50. Nie, W., Tsai, H., Asadpour, R., Blancon, J. C., Neukirch, A. J., Gupta, G., Crochet J.J., Chowalia, M., Tretiak, S. & Wang, H. L., Alam, M.A., High-efficiency solution-processed perovskite solar cells with millimeter-scale grains. *Science* **347**, 522–525 (2015).
51. Wu, Y. et al. Highly compact TiO<sub>2</sub> layer for efficient hole-blocking in perovskite solar cells. *Applied Physics Express* **7**, 052301 (2014).
52. Elumalai, N. K. & Uddin, A. Open circuit voltage of organic solar cells: an in-depth review. *Energy & Environmental Science* **9**, 391–410 (2016).
53. Van Zeghbroeck, B. Principles of semiconductor devices. *Colorado University* (2004).
54. Sharenko, A. & Toney, M. F. Relationships between lead halide perovskite thin-film fabrication, morphology, and performance in solar cells. *Journal of the American Chemical Society* **138**, 463–470 (2015).
55. Sutkovic, F. Photovoltaic technologies and wireless charger, Thesis, *Afyon University* (2015).
56. Park, J.-K. et al. Diffusion length in nanoporous photoelectrodes of dye-sensitized solar cells under operating conditions measured by photocurrent microscopy. *The Journal of Physical Chemistry Letters* **3**, 3632–3638 (2012).
57. Kim, H.-S. et al. High efficiency solid-state sensitized solar cell-based on submicrometer rutile tio<sub>2</sub> nanorod and CH<sub>3</sub>NH<sub>3</sub>PBI<sub>3</sub> perovskite sensitizer. *Nano letters* **13**, 2412–2417 (2013).
58. Kang, S. H., Choi, S. H., Kang, M. S., Kim, J. Y., Kim, H. S., Hyeon, T., & Sung, Y. E. Nanorod-based dye-sensitized solar cells with improved charge collection efficiency. *Advanced Materials* **20**, 54–58 (2008).
59. Adachi, M., Murata, Y., Takao, J., Jiu, J., Sakamoto, M., & Wang, F. Highly efficient dye-sensitized solar cells with a titania thin-film electrode composed of a network structure of single-crystal-like TiO<sub>2</sub> nanowires made by the oriented attachment mechanism. *Journal of the American Chemical Society* **126**, 14943–14949 (2004).
60. Green, M. A., Jiang, Y., Soufiani, A. M. & Ho-Baillie, A. Optical properties of photovoltaic organic-inorganic lead halide perovskites. *The Journal of Physical Chemistry Letters* **6**, 4774– 4785 (2015).

61. Fedeli, P., Gazza, F., Calestani, D., Ferro, P., Besagni, T., Zappettini, A., Calestani, G., Marchi, E., Ceroni, P. & Mosca, R. Influence of the synthetic procedures on the structural and optical properties of mixed-halide (Br, I) perovskite films. *The Journal of Physical Chemistry C* **119**, 21304–21313 (2015).
62. Khatiwada, D., Venkatesan, S., Adhikari, N., Dubey, A., Mitul, A. F., Mohammad, L., Iefanova A., Darling, S.B. & Qiao, Q. Efficient perovskite solar cells by temperature control in single and mixed halide precursor solutions and films. *The Journal of Physical Chemistry C* **119**, 25747–25753 (2015).
63. Tang, Z., Tress, W. & Inganäs, O. Light trapping in thin film organic solar cells. *Materials Today* **17**, 389–396 (2014).
64. Lucas, B. D., Kim, J.-S., Chin, C. & Guo, L. J. Nanoimprint lithography based approach for the fabrication of large-area, uniformly-oriented plasmonic arrays. *Advanced Materials* **20**, 1129–1134 (2008).
65. Saleem, I., Tilakaratne, B. P., Li, Y., Bao, J., Wijesundera, D. N., & Chu, W. K. Cluster ion beam assisted fabrication of metallic nanostructures for plasmonic applications. *Nuclear Instruments and Methods in Physics Research Section B: Beam Interactions with Materials and Atoms* **380**, 20–25 (2016).
66. Liu, Y. Plasmonic metal nanoparticle films for solar cells with ultra-thin absorber layers: Low-temperature synthesis and application. *Ph.D. Thesis, Dissertation, Berlin, Freie Universität Berlin – Germany* (2017).
67. Guerrero, A. Juarez-Perez, E. J., Bisquert, J., Mora-Sero, I. & Garcia-Belmonte, G., Electrical field profile and doping in planar lead halide perovskite solar cells. *Applied Physics Letters* **105**, 133902 (2014).
68. Noel, Nakita K. et al. Enhanced photoluminescence and solar cell performance via Lewis base passivation of organic–inorganic lead halide perovskites. *ACS Nano* **8**, 10, 9815-9821 (2014).